# The JNK signaling links the CNS architectural organization to motor coordination in the *Drosophila* embryo

**Katerina Karkali[1 2 3],George Panayotou[2], Timothy E. Saunders[3] and Enrique Martín-Blanco[1 3 *]**

1. Instituto de Biología Molecular de Barcelona (CSIC), Parc Cientific de Barcelona, Baldiri Reixac 10-12, 08028 Barcelona, Spain

2. BSRC Alexander Fleming, 34 Fleming Street, 16672 Vari, Greece

3. Mechanobiology Institute, 5 Engineering Drive 1, National University of Singapore, 117411 Singapore

* Correspondence to: embbmc@ibmb.csic.es

**ABSTRACT**

In any organism, the construction of the Central Nervous System (CNS) is a complex process that must comply with precise architectural rules. How it is attained and how it affects neural functionality are key issues to solve. In the Drosophila Ventral Nerve Cord (VNC), we uncovered a set of novel robust architectural elements (3D nodes) arranged in a precise pattern responding to a delicate balance on Jun-N-terminal kinase (JNK) signaling activity in specific pioneer neurons. This cascade controls axons and dendrites integrity and, non-autonomously, Fasciclin 2 (Fas 2) expression. A deficit in Fas 2 impairs the VNC architecture and condensation. Remarkably, the coordination of the embryonic motor activity essential for embryo hatching also responds to JNK activity in the same cells. Altogether, our data point to the JNK pathway as an essential element underpinning VNC robustness and reveal critical links between the architecture of the VNC and its functional optimization.

## INTRODUCTION

In higher organisms, behavioral and cognitive functions are directed and coordinated by neural networks [1-3]. Networks interconnect single neural modules, which are comprised of sets of neurons and glial cells with a specific operative design that are arranged in stereotyped structures conserved during evolution [4]. It is still poorly understood: (1) how neural networks acquire their architecturally stable 3D structure; (2) how their spatial organization influences neural functions.

To explore these problems in depth we focused on the *Drosophila* embryonic Central Nervous System (CNS), and in particular in the Ventral Nerve Cord (VNC). The VNC of the *Drosophila* embryo is composed of segmentally iterated ganglia with a stereotyped pattern of neurons organized in a particular 3D array. The neuronal cell bodies are restricted to the cortex, while sensory axons and interneuron projections mostly accumulate in the central neuropile. The positions of these neurons and their projections can be mapped employing segmentally repeated reference points [5]. Cohesive axon bundles build longitudinal connectives and establish transverse commissures [6].

As development proceeds, the VNC autonomously condenses along the anterior/posterior (A/P) axis into a compact bilaterally symmetrical structure. In parallel, the nervous system functionally matures and the sporadic activities of individual motor neurons, interneurons and sensory neurons integrate into specific patterns to direct the motor activities responsible for larval hatching [7]. This maturation into coordinated crawling-like behaviours proceeds autonomously, independent of any sensory input, [8, 9].

Many considerations suggest a direct relationship between the 3D structural organization of the nervous system and its function. Classical neuroanatomy points to evolutionary selection as a key element guiding the spatial organization of cortical areas [10]. Further, in the cortex of vertebrates, large-scale trends in microstructure, connectivity, and gene expression extensively overlap with the spatial distribution of functional processing hierarchies [11]. Last, in pursuit of functional efficiency, neural modules should minimize their wiring cost following the wiring optimization principle postulated by Ramón y Cajal [12]. These costs may arise from metabolic requirements, signal delay and attenuation, and potential guidance defects [13] and would

increase with interneuronal distance [14].

The Jun-N-terminal (JNK) pathway has recently emerged as a conserved regulator for axonal growth and regeneration in the CNS and PNS in mammals, flies and worms [15, 16]. Further, it affects radial cell migration via microtubule-based events [17] and neural tube closure and cortical development in the brain of mouse embryos [18, 19]. Yet, a direct assesment of the role of JNK signaling in the morphogenesis of the CNS has not been performed.

Here we describe the consequences of deregulating the activity of the JNK cascade on the architecture of the VNC and the motor coordination of the *Drosophila* embryo. We first employed a correlative analysis and uncovered an iterated robust pattern of structural elements (3D nodes or cross-pieces). Then we found that the JNK pathway - by directing axon integrity, axonal fasciculation and dendrites formation and non-autonomously modulating Fasciclin 2 (Fas 2) expression - controls the robustness of the VNC architectural organization and its condensation. The attainment of a correct geometry is the result of a delicate balance of JNK signaling activity in specific pioneer neurons. We further found that the precise levels of JNK activity necessary for correct VNC condensation are instrumental in the integration of embryonic motor circuitries. Altering JNK activity levels resulted in a failure in the coordination of muscle contractions and the inability to build the harmonic peristalsis essential for embryo hatching. Altogether, our data elucidates some of the essential molecular and cellular mechanisms underpinning robustness in CNS architecture and highlights the links between its architectural organization and functional optimization.

## RESULTS

### Modular Architecture of the Ventral Nerve Cord (VNC)

The *Drosophila* embryonic VNC is a complex structure with a stereotypical 3D organization and a defined distribution of axonal tracts and neuronal cell bodies. Yet, the elements sustaining its architectural organization are unknown. To shed light on their identity we analyzed the spatial correlations of Fas 2 patterns (**Figures 1A** and **1B**, see also **Movie S1**). Fas 2 is a neural cell adhesion molecule that highlights a subset of the longitudinal axonal connectives, and which

91 loss-of-function leads to complete or partial defasciculation [20]. We uncovered an iterated
92 domain per segment along the A/P axis with a robust 3D geometrical organization (3D node) at
93 an average internodal distance of 28 μm (**Figure 1C**). These nodes positioned slightly anterior to
94 the anterior commissure (see **Figure S1**). At the nodes, the longitudinal connectives organized in
95 three compactly fasciculated units at precise dorso-ventral/medio-lateral positions (**Figure 1D**).
96 Outside the nodes (**Figure 1E**), the fascicles showed an imprecise distribution with a maximal
97 randomness (minimal correlation) at a level in-between the anterior and the posterior
98 commissures. The correlation profiles of the Fas 2 connectives showed not just segmental
99 periodicity (see Experimental Procedures) but a strong structural bias within individual segments
100 (relative difference in the maximum and minimum spatial derivatives of aligned profiles)
101 (**Figure 1F**). The internodal noise increased steeply posteriorly and shallowly anteriorly
102 uncovering a segmental structural polarization (**Figure 1F**).

103 In summary, nodes define topographical domains where the axonal arrangements are sustained
104 from segment to segment in the 3D space. We speculate that nodes correspond to conserved
105 crosspieces holding the architectural organization of the VNC.

106

107 **VNC architecture is modulated by JNK signaling**

108 In *Drosophila*, the JNK activity is moderated by a negative feedback loop implemented by the
109 dual-specificity phosphatase Puckered (Puc). *puc* expression depends on Basket (Bsk), the
110 *Drosophila* homologue of JNK, activity, and Bsk function is inhibited by Puc [21]. Although *puc*
111 expression has been reported in the CNS [22], its function during CNS morphogenesis is
112 unknown. We found that in $puc^{E69}$ loss-of-function mutants, the Fas 2 longitudinal connectives
113 were highly defasciculated and that the intersegmental nerves were unevenly positioned. Axons
114 became irregularly recruited to more medial positions and the Fas 2 signal was frequently
115 relocated to the cell bodies (aCC and pCC neurons) (**Figure 1G** and **Movie S2**). Equivalent
116 defects were also observed for the unrelated $puc^{B48}$ allele (**Figure S2**) [21].

117 Although in *puc*, the Fas 2 fascicles became disorganized on the dorso-ventral/medio-lateral
118 plane (**Figure 1H**), their topographical organization in the A/P axis was robustly conserved and
119 segmental 3D nodes, although more spaced, were still present (**Figure 1I** and **S2**). This increased
120 internodal distance reflected a failure on VNC condensation (on average 18% in $puc^{E69}$ and 39%

121 in *puc*$^{B48}$) (see also direct measurements of the VNC length in **Figure S3**). Further, the A/P
122 structural polarity within segments was also abolished (**Figures 1F**). Puc activity thus appears
123 not to be participating in the establishment of the segmental body plan but into the structural
124 reinforcement of the VNC and its condensation. We further found that in the absence of the
125 negative feedback loop mediated by *puc*, the level of JNK phosphorylation significantly rose in
126 the VNC (**Figure S4**). This increase in JNK activity also correlated with an increment in
127 apoptosis above the VNC characteristic levels (**Figure S4**). In brief, a tight control of JNK
128 signaling appears to be essential for the acquisition of the final architectural organization of the
129 VNC. This control is exerted, at least in part, by Puc, which limits JNK activity and promotes
130 viability.

131

132 **JNK signaling is dynamically regulated in the VNC**

133 When and where is the JNK cascade active in the VNC? To answer this question, we studied the
134 dynamics of *puc* expression, an early readout of JNK activity [21]. A viable Gal4 line under the
135 control of the *puc*$^{E69}$ enhancer [23] identified a segmentally iterated subset of neurons at
136 embryonic stage 17 (**Figures 2A** and **2B**). This pattern originated at stage 13 in a few neurons at
137 the ventral midline (**Figure 2E** and **Movie S3**). No cross-reaction was observed with glial
138 markers (**Figures 2C** and **2D** and [24]). As development progressed, an increased number of
139 neurons within the VNC and at the peripheral nervous system (PNS) expressed *puc*. We
140 identified a minimum consensus of 19 *puc* positive neurons of varying intensity per
141 hemisegment (see diagrams in **Figure 2F** and **Movie S4**).

142 Dual staining of *puc*$^{E69}$ embryos with neuronal markers [Even-skipped (Eve) and Engrailed (En)]
143 identified most of the *puc*-expressing cells (**Figure S5**). *puc* labeled the aCC, pCC, RP2, U1-U3
144 (plus weak/variable expression in U4-U5) and 3 out of the 8/10 EL interneurons. Meanwhile,
145 NL1, NL2, and iVUM5 En+ neurons were *puc* positive. Morphological and positional criteria
146 further enabled the assignment of five other neurons, AD, ADV, dMP2 and 2 VUM En-
147 motoneurons (**Figures 2G** and **2H**). This pattern of *puc*-expressing neurons was largely
148 conserved in *puc*$^{B48}$ (**Figure S6**). Summarizing, *puc* expression was detected from stage 13 in
149 VUMs, pCC and possibly dMP2 neurons at the ventral midline. This expression pattern
150 subsequently expands to diverse inter and motoneurons projecting through the longitudinal
151 connectives and segmental and intersegmental nerves.

152

153 **The level of JNK activity in *puc*-positive neurons controls the VNC architectural**
154 **organization**

155 The altered architecture of the VNC observed in *puc* mutants could be the result of an
156 autonomous malfunction in the CNS, or just a structural consequence of the general disruption of
157 embryo development. To clarify this possibility, we generated JNK loss- or gain-of-function
158 conditions overexpressing $Bsk^{DN}$, a dominant negative form of Basket (Bsk), or $Hep^{CA}$, a
159 constitutively active form of Hemipterous (Hep), the *Drosophila* homologue of the JNK kinase
160 MKK7, in *puc*-expressing cells with different Gal4 lines.

161 The CQ2-Gal4 line drives expression of UAS-linked genes in the U1 to U5 motoneurons (**Figure**
162 **3A**). Neither the inhibition (**Figure 3B**), nor the hyperactivation of the pathway (**Figure 3C**)
163 resulted in any major structural defects. The VNC architecture in both cases (e.g. nodes positions
164 and spatial correlation) was similar to *wt* (**Figures 1A** to **1C**).

165 The RN2-Gal4 line is specifically expressed in the aCC, pCC and RP2 neurons (**Figure 3D**).
166 Interference with JNK signaling in RN2 cells resulted in the disorganization of the Fas 2
167 connectives (**Figure 3E**). The spatial correlations became noisy and irregular, the internodal
168 distances expanded and the condensation of the VNC failed. On the other hand, the
169 hyperactivation of the pathway, mimicking reduced *puc* levels, also strongly affected Fas 2
170 connectives, which kept a juvenile appearance (**Figure 3F**). Although 3D nodes were observed,
171 the internodal distance enlarged and the VNC lengthened.

172 The MzVum-Gal4 line is expressed in a few lateral cells and in the 3 VUM motoneurons (**Figure**
173 **3G**). $Bsk^{DN}$ expression in these cells just slightly affected Fas 2 connectives fasciculation
174 (**Figure 3H**). On the contrary, $Hep^{CA}$ expression resulted in disorganization of Fas 2 connectives
175 and on an increased noise in spatial correlations (**Figure 3I**). Internodal distances also became
176 larger and the VNC does not condense.

177 Altogether these data suggest that the level of JNK activity must be carefully tuned in the early-
178 specified aCC, pCC, and RP2 pioneers and VUM neurons to facilitate the robust architectural
179 organization of the VNC.

180

181

182 **JNK signaling modulates Fasciclin 2 levels in the developing VNC**

183 The non-autonomous impact of JNK signaling from local sources on global VNC morphogenesis
184 requires the propagation of the cellular responses to JNK. While direct instructive
185 communication by growth factors or neurotransmitters can be an important determinant of
186 structural changes [25], adhesion molecules also stand as key elements for large-scale processes
187 [26].

188 We explored whether the global effects of *puc* on structural robustness could be associated to Fas
189 2 deregulation or subcellular mislocalization. Fas 2 has been implicated in fasciculation by
190 promoting adherence between growing axons [27]. By quantifying Fas 2 integrated densities in
191 *wt*, $puc^{E69}$, and $puc^{B48}$ embryos (**Figures 4A** to **4C**) we found that in all conditions it was
192 enriched at the 3D nodes, which was consistent with their high axonal density. Fas 2 expression
193 was reduced by 50% in the absence of Puc (at high JNK activity) (**Figure 4D**). This reduction
194 was systemic and could not be assigned to individual domains within the VNC. In agreement, the
195 quantification of protein levels in stage 16 embryo extracts showed a global reduction of Fas 2
196 expression in mutant conditions (**Figure 4E**).

197 These analyses support a model in which the global architectural organization of the VNC is
198 influenced by the proper deployment of Fas 2 in response to the controlled activity of the JNK
199 pathway in, at least, the aCC, pCC, RP2 and VUMs neurons.

200

201 **JNK signaling influences the axodendritic organization of *puc*-expressing neurons**

202 To investigate the structural origins of the effects of JNK signaling on the overall architectural
203 organization of the VNC we monitored the axonal integrity and dendritic arborization of *puc*-
204 expressing neurons. We observed that the overexpression of $Hep^{CA}$ in RN2 (aCC, pCC and RP2)
205 cells led to the local disorganization of the tissue affecting axonal morphologies and dendrites
206 number and organization.

207 The aCC is a motoneuron whose axon gets incorporated into the intersegmental nerve (ISN) and
208 proceeds laterally to innervate the dorsal muscle DA1 [28]. Its dendritic arbor develops in a
209 distinct region of the ISN myotopic dendritic domain and consists of 8-10 dendrites [29] of an
210 average length of 4 μm (**Figure 5A**). The pCC is a medially-located interneuron whose axon
211 extends ipsilaterally in an anterior direction [30]. Finally, the RP2 motoneuron axonal trajectory

212 proceeds through the posterior root of the ISN and forms endings on all dorsolateral and dorsal
213 internal muscles [28, 31]. Accordingly, the RP2 develop its dendrites into the region of the
214 neuropile that represent its targets in the myotopic map [32]. Between 7 and 9 dendrites of an
215 average length of 4 μm branching out of the RP2 axon can be regularly found (**Figure 5A**).
216 Upon overexpression of $Hep^{CA}$, the cell bodies of the aCC, pCC and RP2 neurons were
217 frequently misplaced and came together towards the midline (compare **Figures 5A** and **5B**). The
218 appearance of their axons was affected; they thicken and became slack, while their length
219 increased (for pCC and the RP2) (**Figures 5C** and **5D**). $Hep^{CA}$ overexpression also affected the
220 density and length of dendrites. Both for aCC and RP2, dendrites numbers were reduced by half
221 (**Figure 5E**) and they became longer reaching up to 15 μm of length (**Figure 5F** and **Movie S5**).
222 Our data show that altering JNK activity levels led autonomously to structural and, potentially,
223 transmission defects in motoneurons. These faults along the loss of the adhesive capabilities of
224 the tissue, consequence of the reduction of Fas 2 levels, may be responsible in certain degree of
225 the architectural failures of the VNC as a whole, including its lack of condensation.
226
227 **The VNC architectural organization is essential for embryonic motor coordination**
228 To determine the functional relevance of the robust architectural organization of the VNC, we
229 analyzed the process of maturation of embryonic motor patterns [7, 8] (**Figure 6A** and **6B**) (see
230 Experimental Procedures, **Figure S7** and **Movie S6**). The *Drosophila* larva moves by peristaltic
231 crawling and even before hatching, embryos execute forward and backward waves of peristalsis.
232 These waves require the coordinated, bilaterally symmetrical, contraction of the thoracic and
233 abdominal muscles [7, 33]. We found that embryonic movements began with isolated unilateral
234 brief muscle twitches, sporadic head pinching events and sequences resembling incomplete
235 peristalsis (stage A). This stage was followed by a prolonged resting period (stage B)
236 occasionally interrupted by uncoordinated single contractions involving one or few segments. As
237 development proceeds multi-segmental events arose with incomplete and complete peristalsis
238 (stage C). These events then became less and less frequent until they ceased completely into a
239 short resting period (stage D). Last, violent head movements and multiple peristaltic waves took
240 place (stage E) leading to the rupture of the viteline membrane and larva hatching (**Figure 6C**
241 and **6D** and **Movie S7**). These stages of stereotyped length closely recapitulate previous reports
242 (Crisp et al., 2008). In the absence of *puc* ($puc^{E69}$), the developmental progression of motor

243 patterns was interrupted and embryos remained indefinitely in an immature stage (A)
244 characterized by occasional unilateral twitches and incomplete peristalsis, (**Figure 6E** and **6F**
245 and **Movie S8**).

246 Muscle integrity and functionality were not affected in *puc* embryos. Yet, the systemic failure of
247 motor coordination could still be the indirect consequence of non-defined events resulting from
248 an overall increase of JNK activity in *puc* mutants. To evaluate this possibility we overexpressed
249 $Hep^{CA}$ in RN2 (**Figure 7A** and **7B**) or MzVum (**Figure 7C** and **7D**) cells. In both cases, an
250 excess of JNK activity in just the *puc*-expressing neurons resulted in an equivalent phenotype to
251 that observed in $puc^{E69}$ mutants. Only occasional unilateral twitches and head pinches and
252 infrequent incomplete peristalsis were observed in either condition. Therefore, the motor defects
253 in *puc* appear to be a direct response to loss of Puc activity in *puc*-expressing neurons.

254 Would the loss of motile synchrony be related to the aberrant architectural organization of the
255 VNC or to a signaling defects consequence of altering JNK activity in *puc*-expressing neurons?
256 Some of these *puc*+ cells are motoneurons and in the absence of a correct level of JNK activity,
257 their signaling capability might be impaired. To test this possibility, we studied the axonal
258 transport of synaptotagmin, a key component of synaptic vesicles in the intersegmental nerve
259 [aCC and RP2 (RN2-Gal4) (**Figure 7E**) and VUM motoneurons (MzVum-Gal4) (**Figure 7F**)]
260 (see Experimental Procedures and **Movie S9**). Both in RN2 and MzVum axons, synaptotagmin
261 (synaptic vesicles) moved at a speed of around 0,7 μm/s with a tracking lifetime of 50 s per
262 event. Particles densities (frequency of events) were larger for aCC and RP2 (0,3 N/μm) than for
263 VUMs (0,2 N/μm). No differences were observed between anterograde and retrograde transport.
264 Next, particle transport was analyzed upon co-expression of $Hep^{CA}$ in RN2 and MzVUM cells.
265 Synaptotagmin transport behavior was largely unaffected (**Figures 7G to 7L)** which indicate that
266 microtubules, motor systems and synaptic vesicles transport remained fully functional. As for the
267 wild type, we could not distinguish differences between anterograde and retrograde transport.

268 In conclusion, synaptotagmin and, potentially, neurotransmitters transport appeared not to be
269 disturbed by the deregulation of JNK activity. These results suggest that the main function of the
270 attenuation of the JNK pathway in the VNC by Puc is mainly structural ensuring its robust
271 architectural organization. The embryonic motor coordination would be a foreseeable
272 consequence.

273

## DISCUSSION

### The VNC attains a robust Architectural Organization

The complex nervous system of bilaterians is thought to have emerged from an ancient, diffuse nerve plexus [34] that evolved into a segmented structure polarized along the Anterior/Posterior (A/P) axis [35]. 'Homologous' neurons functioning in different body segments are serially repeated and conserved across species in other arthropods. We have found that this conservation at the cellular level is reflected in a unique architectural pattern. Structurally, the VNC of the *Drosophila* embryo is composed of segmentally iterated ganglia with well-structured commissures and well-defined segmental and intersegmental nerves. Fasciculated axons (those expressing Fas 2) become robustly organized in 3D at one anchoring position (nodes) per segment slightly anterior to the connecting anterior commissure (**Figure 1** and **S1**). These commissures contain bundles of primary neurites where many synapses are made. A likely reason for this robust organization is that it responds to conserved architectural needs in terms of mechanics and physical balance [34, 36]. We speculate that in architectural terms the connectives may work as structural beams and that nodes help to distribute evenly any load from compression, tension or shear arising as the VNC is built (or that it may suffer once functional). This backbone will support the accumulated cargo of neuronal cell bodies, assuring that the elements required to fulfill neural functions will be robustly established. Yet, the Fas 2 connectives may not be the only element holding the tensional network of the VNC as the global axonal landscape of the embryo includes many other elements not expressing Fas 2.

### The JNK signaling modulates the 3D structure of the Nervous System

During the morphogenesis of the nervous system, both neurons and glia grow, change shape and accommodate overtime to establish a mechanically equilibrated and precisely organized 3D structure. Doing so, they generate - and also become the target of - forces and tensional stresses. It has been suggested that the compaction and clustering of cells in neural modules could be the result of the spatio-temporal regulation of mechanical tension in and along axons [37]. Indeed, tension forces contribute to neuronal morphology and connectivity [38], neurite connections

304 stabilization [37] and remodeling of neuronal processes and functional wiring [39]. Yet, the
305 information on how the tensional and topographical landscape of the nervous system is
306 implemented is scarce. A candidate to modulate neural structural organization and function and,
307 eventually, tension within the CNS is the stress activated JNK cascade [40].

308 The robust structural organization and the condensation of the VNC appear to be associated
309 events and they are both regulated by JNK activity. In *puc* mutants, Fas 2 bundles defasciculate,
310 the overall shape of the neuropile is affected, and the VNC fails to condense (**Figures 1** and **S3**).
311 3D nodes are still present at the right position within segments but the internodal distances are
312 enlarged. Remarkably, the comparison of spatial correlations profiles indicate that in each
313 segment the shrinkage of the domain immediately posterior to the nodes (roughly covering the
314 anterior commisure) is key for VNC condensation. If these iterated narrowings are temporally or
315 spatially (segmentally) regulated or if they are the only ones or just major participants in the
316 condensation process remains to be studied. In any case the regulated attenuation of the JNK
317 signaling cascade is essential.

318 In *Drosophila*, the pioneer neurons are specified and singled out at stage 9 and initiate
319 axonogenesis around stage 11 [30]. JNK activity, in parallel, builds up in the CNS and is
320 detected (*puc* expression) in the midline VUMs, and the pCC and dMP2 early pioneers (**Figure**
321 **2**). This temporal correlation argues that the major aberrations in fasciculation observed in *puc*
322 embryos may result from pioneering defects. Potentially, inaccurate axonogenesis of pioneers
323 could impact non-autonomously in the fasciculation of axons from late neurons that encounter an
324 altered guidance landscape. Indeed, we observed that autonomously increasing JNK activity in a
325 few early-specified neurons or in midline pioneers (RN2 and MzVum positive neurons) affects
326 their axons lengths and paths and their dendritic arborizations (**Figure 5**) preceeding widely
327 spread fasciculation defects. The failure of the VNC condensation may have the same origin.
328 VNC defects are remarkably similar upon reduction or increase in JNK function, indicating that
329 precision in the control of its contribution is essential. The negative feedback loop mediated by
330 *puc* would thus be a main factor in this tight spatio-temporal regulation.

331 How JNK activity levels would impinge in the architectural organization of the VNC? Fas 2 is a
332 neural cell adhesion molecule that highlights a subset of the longitudinal axonal connectives, and
333 which loss-of-function leads to complete or partial defasciculation [20]. The regular segmental
334 arrangement of Fas 2 nodes suggests they are important elements for the global stabilization of

335 the VNC structure. Defective node formation or alterations in neurons adhesion properties (e.g.
336 by Fas 2 downregulation) would weaken the structural scaffold. It has been shown that tension,
337 alongside cell adhesion and neurotransmitter-dependent signaling is necessary for axonal growth
338 and transport, it also promotes neurites maturation and supports dendrites development in
339 different models [41]. The disassembly of Fas 2 connectives and architectural rearrangements in
340 *puc* mutants are associated with a strong reduction of Fas 2 levels. Remarkably, The Fas 2
341 reduction is not a consequence of its relocation (e.g. node to internode) but instead to its systemic
342 downregulation (**Figure 4**). Interestingly, an equivalent link between JNK signaling and Fas 2
343 has been observed in the pruning of mushroom body gamma neurons axons. Bsk promotes
344 pruning by reducing the membrane levels of Fas 2 [42].

345 Altogether, our data suggest that the activation of *puc* expression by JNK in early-specified
346 pioneer neurons (aCC, pCC, RP2, dMP2 and VUMs) results in the downregulation of the
347 pathway, and an overall increase in Fas 2 levels. Fas 2 would be essential for proper structural
348 development [20]. A deficit in Fas 2 would affect the fasciculation of the axons of primary
349 neurons, leading to secondary bundling defects resulting in a general reduction in spatial
350 correlations across the whole axonal network of the neuropile. Failure to properly fasciculate, the
351 misrouting of axonal paths and alterations in dendritic arborizations would eventually affect both
352 the architectural organization and the tensional balance of the VNC, ultimately impeding its
353 condensation (**Figure 8**).

354

355 **Coordination of motor activities by JNK signaling**

356 In the *Drosophila* embryo, motor networks become active very early and isolated twitches and
357 unilateral waves of contraction occur prior to the generation of propagated action potentials by
358 neurons [43]. The early muscle contractions are thus myogenic in origin [7]. The elaborated
359 rhythmic coordination of motor function and its optimization are, however, the consequence of a
360 gradual maturation dependent on a functional Central Pattern Generator (CPG) [44]. In other
361 words, the invariant pattern of muscle contraction that constitutes a full peristaltic wave depends,
362 besides specific motoneuron activities, on the development of excitatory and inhibitory
363 interactions accross segments.

364 Does the geometrical and architectural organization of the VNC have any functional

365 significance? Which are the consequences of acquiring its precise shape and size? Our data
366 strongly advocate for a close relationship between the VNC axial condensation and the
367 development of a functional CPG and the acquisition of coordinated motor functions. Both, in
368 different *puc* alleles or after overexpressing $Hep^{CA}$ in the aCC, pCC, RP2 and VUM neurons,
369 when the robustness of the VNC organization is compromised, the embryo's motor coordination
370 becomes interrupted. Mutant embryos shake their muscles at low pace continuously and stay
371 alive for up to 24 h but do not hatch. Their muscles motility patterns can be best described as
372 uncoordinated individual segments contractions, where left and right hemisegments are often out
373 of phase and peristaltic waves are absent. These animals do not proceed beyond the early stage
374 of spontaneous twitches (A) observed in wild type embryos. While this outcome could be
375 explained as an indirect result of signaling defects associated to odd dendritic arborizations [45]
376 (**Figure 5**), we postulate that they are most probably linked to the incomplete compaction of the
377 VNC (**Figures 1** and **3**).

378 It is well established that correlated spontaneous activities [46] repeatedly and persistently
379 stimulating postsynaptic cells will result in long-term synapse strengthening (long-term
380 potentiation [LTP]) [47]. These spontaneous activity patterns are known to propagate, ensuring
381 that the connections between neighboring cells are strengthened, whereas those from more
382 distant ones are lost [48]. Thus, functional interconnectedness will only be reached by bringing
383 cells in close proximity leading to wiring optimization [12]. We hypothesize that these principles
384 will be followed during the condensation of the VNC ensuring the coordination of motor
385 activities. Several arguments support this premise. The muscle activity phenotype observed for
386 *puc* closely resembles that of *glial cells missing* (*gcm*). In *gcm*, neurons are unaffected but most
387 classes of glial cells are lost and VNC condensation does not take place. Peristaltic waves are
388 absent and uncoordinated movements are continuous [33]. Further, the activation or ablation of
389 the Even-skipped+ EL interneurons (Eve/Evx) disrupt the bilaterally symmetrical muscle
390 contractions in the larvae [49]. These ELs make direct presynaptic contacts to the contralateral
391 dorsal-projecting motoneurons RP2, U1, and U2. Amongst these, we found the RP2 to be key in
392 directing the structural organization of the VNC (**Figure 3**) and for motor coordination (**Figure**
393 **6**). The ELs and the dorsal projecting motoneurons they innervate are nearly all *puc* expressing
394 neurons (**Figure 2**). It will be of interest in the future the analysis of the EL sensorimotor circuit
395 and its signaling capabilities upon perturbation of JNK activity.

396 The principle of wiring optimization also likely applies to postembryonic development. As a
397 *Drosophila* larva develops, its body wall surface area grows by two orders of magnitude [50]. To
398 accommodate such physiological changes, mechanosensory neurons must extend their dendrites
399 to maintain receptive fields [51], while larval motor neurons add more synapses to maintain
400 functional responses in much larger muscles [50, 52]. Interestingly, during scaling, the likelihood
401 of synaptic contact between nearby neurons is stereotyped and cell type-specific [53]. In this
402 scenario, a post-synaptic neuron can only connect to spatially nearby pre-synaptic sites. This
403 local propensity to form stable synapses with a nearby cell type is preserved across development.
404 The application of correlative geometrical and mechanical analyses in combination with cell
405 type-specific genetic interference will allow wiring optimization to be tested across different
406 circuits and to better elucidate the detailed mechanisms underlying the CNS structural
407 development.
408
409
410 **EXPERIMENTAL PROCEDURES**
411
412 **Drosophila strains**
413 The following stocks were used:
414 w; *puc*$^{E69}$*LacZ/TM3, twi-GFP* [21]
415 *w; puc*$^{B48}$*LacZ/ TM3, twi-GFP* [21]
416 w; UAS-GFP; *puc*$^{E69}$*I*–Gal4/TM6B [23]
417 w; UAS-GFP; *puc*$^{B48}$–Gal4/TM6B [23]
418 *w[1118], P{w[+mC]=UAS-bsk.DN}2* (BDSC #6409)
419 *w[*]; P{w[+mC]=UAS-Hep.Act}2* (BDSC #9306)
420 *P{GawB}elav[C155]* (BDSC #6923)
421 *w[*]; P{w[+mC]=eve-GAL4.RN2}T, P{w[+mC]=UAS-mCD8::GFP.L}; P{w[+mC]=eve-*
422 *GAL4.RN2}G, P{w[+mC]=UAS-mCD8::GFP.L} (*Dr. Irene Miguel-Aliaga)
423 y*[1] w[*];P{w[+mC]=CQ2-GAL4}O, P{w[+mC]=UAS-mCD8::GFP.L}LL6* (BDSC #7465)

424 *w[*] P{w[+mW.hs]=GawB}MzVUM; P{y[+t7.7] w[+mC] = 10xUAS-IVS-mCD8::GFP}attP40*
425 *(*Dr. Irene Miguel-Aliaga)

426 *w[*]; G203:UAS-TNT; ZCL2144* (Dr. Matthias Landgraf)

427 *w[*]; ; ZCL2144* (Dr. Matthias Landgraf)

428 *w*; P{UAS-syt.eGFP}2* (BDSC #6925)

429 In all cases, unless otherwise stated, embryos of the *w1118* strain served as controls.

430

431 **Immunohistochemistry**

432 Immunostaining of flat-prepped stage 16 *Drosophila* embryos was performed using the
433 following primary antibodies: mouse anti-Fas 2 (1:100, clone 1D4, DHSB), mouse anti-axons
434 CNS (1:100, BP 102, DHSB), mouse anti-Futsch (1:1000, 22c10, DHSB), rabbit anti-phospho-
435 JNK ($Thr^{183}$ / $Tyr^{185}$) (1:100, Cell Signaling #9251), rabbit anti-Dcp-1 (Asp216) (1:100, Cell
436 Signaling #9578), rabbit anti-GFP tag polyclonal (1:600, Thermo Fisher Scientific), rat anti-Elav
437 (1:1000, clone 7E8A10, DHSB), mouse anti-Repo (1:100, clone 8D12 DHSB), mouse anti-Even-
438 skipped (1:100, clone 3C10, DHSB), and mouse anti-Engrailed (1:100, clone 4D9, DHSB).

439 The secondary antibodies used for detection were: Goat anti-Rabbit IgG (H+L), Alexa Fluor 488
440 conjugate (A-11008), Goat anti-Rabbit IgG (H+L) Alexa Fluor 555 conjugate (A-21428), Goat
441 anti-Mouse IgG (H+L) Alexa Fluor 488 conjugate (A-11001), Goat anti-Mouse IgG (H+L)
442 Alexa Fluor 555 conjugate (A-21422) and Goat anti-Rat IgG (H+L) Alexa Fluor 555 conjugate
443 (A-21434). All secondary antibodies were used in a dilution of 1:600 and were from Invitrogen.

444

445 **Sample preparations for immunodetection and image acquisition**

446 *Drosophila* embryo dissections for generating flat preparations were performed according to
447 [28]. Briefly, flies maintained in apple juice-agar plates at 25ºC were synchronized by repetitive
448 changes of the juice-agar plate, with a time interval of 1.5 hours. All embryos laid within this
449 time window were aged for approximately 22 hours at 18ºC, or until reaching mid-stage 16 (3-
450 part gut stage). At this point embryos were dechorionated with bleach for 1 min, poured into a
451 mesh and rinsed extensively with water. For dissection, embryos were transferred with forceps
452 on the surface of a small piece of double sided tape, adhered on one of the sides of a poly-L-
453 Lysine coated coverslip. After orienting the embryos dorsal side up and posterior end towards

454 the center of the coverslip, the coverslip was flooded with saline (0.075 M Phosphate Buffer, pH
455 7.2). Using a pulled glass needle the embryos were manually de-vitellinized and dragged to the
456 center of the coverslip, where they were attached to the coated glass with their ventral side down.
457 An incision on the dorsal side of the embryo was performed using the glass needle from the
458 anterior to the posterior end of the embryo. The gut was removed by mouth suction and blowing
459 stream of saline was used to flatten their lateral epidermis. Tissue fixation was done with 3.7 %
460 formaldehyde in saline for 10 minutes at room temperature. After this point standard immuno-
461 staining procedures were followed.

462 In the single case (**Figure S3**) where whole mount embryos were immunostained, embryo
463 fixation and de-vitalinization was done according to [54]. Both whole mount and flat-prepped
464 immunostained embryos were mounted in Vectashield anti-fading medium (Vector Laboratories,
465 USA).

466 Image acquisition was performed on a Zeiss LSM 700 inverted confocal microscope, using a 63
467 x oil objective lens (NA 1.4). Z-stacks spanning the whole VNC thickness were acquired
468 applying optimal, with respect to pinhole diameter, sectioning with a step size that varied
469 between 0.2 – 0.6 μm. Image processing was performed with Fiji [55].

470

471 **Live imaging**

472 Dechorionated stage 14 embryos were glued ventral side down on a MatTek glass bottom dish
473 and they were covered with S100 Halocarbon Oil (Merck) to avoid desiccation. Image
474 acquisition was performed on a Zeiss LSM 700 inverted confocal microscope, using a 25 x oil
475 objective lens (NA 0.8). Z-stacks spanning the whole VNC thickness and with a 2 μm step size
476 were acquired every 6 minutes for a total of 8 hours. Processing of time-lapse data was done with
477 Fiji [55].

478

479 **Image analysis**

480 Image analysis and quantification of fluorescence intensity were performed using Fiji [55]. In
481 immunostainings where quantification of the fluorescent intensity was required, extra care was
482 taken so that the same antibody batch was used for staining embryos of different genotypes,
483 while identical confocal acquisition settings were applied.

484 For calculating the average integrated density of Fas 2 signal in an image, regions of interest
485 (ROIs) of fixed size were measured at the nodes and internodes positions. Average Integrated
486 Density values obtained by measuring ROIs in several animals (n stated in Figure legends) were
487 then pooled for calculating the mean value as well as standard deviations. For those cases where
488 the quantification of integrated density was performed on a segment basis, the measured values
489 represent the raw integrated density, since the area measured slightly varies in between animals.

490

491 **Statistical analysis**

492 All statistical analyses were performed using GraphPad Software (GraphPad Software Inc., La
493 Jolla, CA, USA). In all cases one sample t test was performed and probability values $p<0.05$
494 were considered as significant.

495

496 **Correlations Data analysis**

497 Images were scaled to be isotropic in all axes. Deconvolution was found to not significantly
498 improve the image correlation. Viewed along the antero-posterior axis, images were cropped to
499 include only the VNC, and then the VNC was differentiated into 50 bins, corresponding to 1,65
500 μm length each. Within each bin, a maximum intensity projection was performed along the
501 included (typically eleven) planes. The Matlab function *imregister* was then used to perform the
502 image registration for both inter- and intra- embryo correlations. The optimizer for *imregister*
503 was defined with multimodal metric, tolerance of $10^{-6}$ and 500 iterations. Before image
504 registration, the center of mass of the two images was aligned so to maximize image overlap.
505 The code was run on a PC with 128 Gb memory and in the most demanding case (full embryo
506 correlation: 50 x 50 = 2500 correlations) took around one hour per sample.

507 To create the image correlation traces, the regions of high correlation (e.g. as identified by
508 arrows in **Figure 1**) were manually identified and then plotted considering the mean correlation
509 along ± 1 row in the correlation matrices. The diagonal values were ignored. Traces were offset
510 along AP axis to ensure maximum overlap of peaks in the region 25-57 μm to aid comparison
511 between different datasets. In all figures, individual profiles are plotted in gray, with the mean
512 (black) and ± 1 standard deviation (red) shown. For each maximum in the spatial correlation
513 profile, and a subset of data was sliced that lay between the two minima at either side. Then, we

514 created *in silico* data from the real experimental data points - i.e. each *in silico* data point was
515 drawn from a distribution defined by the mean and standard deviation in the samples. We
516 determined the best linear fit to each *in silico* data set and repeated 500 times to find the average
517 gradient fit. This was a robust way to find the steepness as it accounts for experimental noise. To
518 compare between datasets, we defined the variable

519 r = (max(gradient) - abs(min(gradient))) / [(max(gradient)+abs(min(gradient)))/2]

520 *i.e.* the difference / mean.

521

522 **Muscle contraction analysis**

523 Stage 17 embryos carrying the G203, ZCL2144 or both GFP muscle markers were dechorionated
524 and mounted in halocarbon oil (3:1 mix of S700 and S27) following standard procedures. Muscle
525 contractions were monitored at the embryo's middle plane, using a 25 X oil immersion lens (N.A
526 0.8, Imm Korr DIC M27) in a Zeiss LSM780 confocal microscope. For each acquisition 1000
527 frames were obtained with a scanning speed of 200 msec per frame with a time interval between
528 acquisition cycles of 15 minutes. Muscle activity was monitored up to embryo's hatching or for a
529 total of 12 hours at room temperature. For the experiments where $Hep^{CA}$ over-expression in RN2
530 and MzVum neurons was required, both control and $Hep^{CA}$ overexpressing embryos were filmed
531 at 29$^{o}$C for equal time periods. Post-imaging, movies were processed with Fiji [55] and
532 Kymographs were generated using the Fiji plugin KymoResliceWide.

533

534 **Axonal Trafficking**

535 To examine axonal trafficking, stage 17 embryos expressing UAS-Syt-GFP were dechorionated
536 and mounted laterally in halocarbon oil (3:1 mix of S700 and S27) for live imaging. Synaptic
537 vesicle transport was monitored in the medial part of the Inter-Segmental Nerve (ISN) using a 40
538 X oil immersion lens (N.A 1.3, Oil DIC M27) in a Zeiss LSM780 confocal microscope. A
539 constant frame size of 512x100 pixels, with an XY zoom of 6 and a recording line spacing of 2
540 were routinely employed. Single plane movies were acquired with a scanning speed of 1.11 sec,
541 with 1 sec interval for a total of 60 cycles. All movies were processed with Fiji and Kymographs
542 were generated using the Fiji plugin KymoResliceWide.

The Mean Velocity and the Lifetime parameters for each particle were calculated from the Kymographs as follows. The particles trajectories were traced and saved as independent ROIs. The XY coordinates for each ROI were then extracted using the getSelectionCoordinates function in Fiji of the custom made “Macro coordinates.ijm” shown below:

```
run("Fit Spline", "straighten");
  getSelectionCoordinates(x, y);
  x2=0; y2=0; distance=0;
  for (i=0; i<x.length; i++) {
      if (i>0) {
         dx = x[i] - x[i-1];
         dy = y[i] - y[i-1];
         distance = sqrt(dx*dx+dy*dy);
      }
      print(i, x[i], y[i], distance);
  }
```

These XY coordinates represent the particles displacement in both space (X values) and time (Y values), thus permitting the calculation of Mean Velocity and Lifetime.

**Analysis of Axonal and dendrite morphology by Segmentation**

To describe the axonal and dendrite morphology of the RN2-Gal4 positive neurons, we analyzed images of flat-prepped embryos immunostained against GFP and Fasciclin II using the Simple Neurite Tracer Fiji plugin [56]. Image segmentation by this tool allows a semi-automated tracing of axons and dendrites in 3D, providing measurements of total axonal and dendrite length, as well as of dendrite number directly from skeletonized images.

571 **Western Blotting**

572 Dechorionated stage 16 embryos of the *puc*$^{E69}$*LacZ / TM3, twi-GFP* and *puc*$^{B48}$*LacZ / TM3, twi-*
573 *GFP* lines were used for generating whole embryo extracts for western blot analysis. In detail,
574 homozygous embryos were separated from their balanced siblings under a fluorescent dissecting
575 scope based on the *twi-GFP* expression. Approximately 100 embryos of each type were fully
576 homogenized in 100 μL of iced cold RIPA buffer, supplemented with Protease Inhibitors
577 (Protease Inhibitor Cocktail Tablets, Roche Life Sciences). Subsequently, the extracts were
578 centrifuged at 3500 g for 15 minutes at 4ºC and the supernatants were collected. Total protein
579 concentration in the lysates was determined by Bradford assay (Bio-Rad) and 30 μg of sample
580 were analyzed in a 10 % SDS-PAGE. Proteins were blotted on Protran nitrocellulose membrane
581 (Whatman) while the antibodies employed were: anti-Fas 2 (1:1000, clone 1D4, DSHB) and
582 Pan-actin (1:1000, Cell Signaling). The ECL Plus chemiluminescent substrate (Pierce, Thermo
583 Fisher Scientific) was used for antibody detection. Western Blot signal quantification was
584 performed with Fiji by measuring the average density of each band.

585

586

587 **REFERENCES**

588

589 1. Leise EM. Modular construction of nervous systems: a basic principle of design for
590 invertebrates and vertebrates. Brain research reviews. 1990;15(1):1-23.

591 2. Chen BL, Hall DH, Chklovskii DB. Wiring optimization can relate neuronal structure
592 and function. Proceedings of the National Academy of Sciences of the United States of
593 America. 2006;103(12):4723-8.

594 3. Redies C, Puelles L. Modularity in vertebrate brain development and evolution.
595 BioEssays. 2001;23(12):1100-11.

596 4. Sporns O, Betzel RF. Modular Brain Networks. Annu Rev Psychol. 2016;67:613-40.

597 5. Landgraf M, Sanchez-Soriano N, Technau GM, Urban J, Prokop A. Charting the
598 Drosophila neuropile: a strategy for the standardised characterisation of genetically
599 amenable neurites. Developmental biology. 2003;260(1):207-25.

600 6. Technau GM. Brain development in Drosophila melanogaster: Springer
601 Science+Business Media, LLC - Landes Bioscience; 2008.

602 7. Crisp S, Evers JF, Fiala A, Bate M. The development of motor coordination in
603 Drosophila embryos. Development. 2008;135(22):3707-17.

604 8. Crisp SJ, Evers JF, Bate M. Endogenous patterns of activity are required for the
605 maturation of a motor network. The Journal of neuroscience. 2011;31(29):10445-50.

606 9. Suster ML, Bate M. Embryonic assembly of a central pattern generator without
607 sensory input. Nature. 2002;416(6877):174-8.

608 10. Huntenburg JM, Bazin PL, Margulies DS. Large-Scale Gradients in Human Cortical
609 Organization. Trends Cogn Sci. 2018;22(1):21-31.

610 11. Huntenburg JM. A core organizing axis of the human cerebral cortex: Freie
611 Universität Berlin; 2018.

612 12. Cajal SRy. Textura del Sistema Nervioso del Hombre y de los Vertebrados. Madrid,
613 Spain: Nicolas Moya; 1899.

614 13. Tessier-Lavigne M, Goodman CS. The molecular biology of axon guidance. Science.
615 1996;274(5290):1123-33.

616 14. Chklovskii DB, Koulakov AA. Maps in the brain: what can we learn from them?
617 Annual review of neuroscience. 2004;27:369-92.

618 15. Srahna M, Leyssen M, Choi CM, Fradkin LG, Noordermeer JN, Hassan BA. A signaling
619 network for patterning of neuronal connectivity in the Drosophila brain. PLoS biology.
620 2006;4(11):e348.

621 16. Koch M, Nicolas M, Zschaetzsch M, de Geest N, Claeys A, Yan J, et al. A Fat-Facets-
622 Dscam1-JNK Pathway Enhances Axonal Growth in Development and after Injury. Front Cell
623 Neurosci. 2017;11:416.

624 17. Hirai S, Banba Y, Satake T, Ohno S. Axon formation in neocortical neurons depends
625 on stage-specific regulation of microtubule stability by the dual leucine zipper kinase-c-Jun
626 N-terminal kinase pathway. The Journal of neuroscience. 2011;31(17):6468-80.

627 18. Kuan CY, Yang DD, Samanta Roy DR, Davis RJ, Rakic P, Flavell RA. The Jnk1 and Jnk2
628 protein kinases are required for regional specific apoptosis during early brain
629 development. Neuron. 1999;22(4):667-76.

630 19. Waetzig V, Herdegen T. Neurodegenerative and physiological actions of c-Jun N-
631 terminal kinases in the mammalian brain. Neuroscience letters. 2004;361(1-3):64-7.

632 20. Lin DM, Fetter RD, Kopczynski C, Grenningloh G, Goodman CS. Genetic analysis of
633 Fasciclin II in Drosophila: defasciculation, refasciculation, and altered fasciculation. Neuron.
634 1994;13(5):1055-69.

635 21. Martin-Blanco E, Gampel A, Ring J, Virdee K, Kirov N, Tolkovsky AM, et al. puckered
636 encodes a phosphatase that mediates a feedback loop regulating JNK activity during dorsal
637 closure in Drosophila. Genes & development. 1998;12(4):557-70.

638 22. Martin-Blanco E. Regulatory control of signal transduction during morphogenesis in
639 Drosophila. The International journal of developmental biology. 1998;42(3):363-8.

640 23. Pastor-Pareja JC, Grawe F, Martin-Blanco E, Garcia-Bellido A. Invasive cell behavior
641 during Drosophila imaginal disc eversion is mediated by the JNK signaling cascade. Dev
642 Cell. 2004;7(3):387-99.

643 24. Shklover J, Mishnaevski K, Levy-Adam F, Kurant E. JNK pathway activation is able to
644 synchronize neuronal death and glial phagocytosis in Drosophila. Cell death & disease.
645 2015;6:e1649.

646 25. Foty RA, Steinberg MS. The differential adhesion hypothesis: a direct evaluation.
647 Developmental biology. 2005;278(1):255-63.

648 26. Amack JD, Manning ML. Knowing the boundaries: extending the differential
649 adhesion hypothesis in embryonic cell sorting. Science. 2012;338(6104):212-5.

650 27. Grenningloh G, Rehm EJ, Goodman CS. Genetic analysis of growth cone guidance in
651 Drosophila: fasciclin II functions as a neuronal recognition molecule. Cell. 1991;67(1):45-
652 57.

653 28. Landgraf M, Bossing T, Technau GM, Bate M. The origin, location, and projections of
654 the embryonic abdominal motorneurons of Drosophila. The Journal of neuroscience.
655 1997;17(24):9642-55.

656 29. Furrer MP, Vasenkova I, Kamiyama D, Rosado Y, Chiba A. Slit and Robo control the
657 development of dendrites in Drosophila CNS. Development. 2007;134(21):3795-804.

658 30. Jacobs JR, Goodman CS. Embryonic development of axon pathways in the Drosophila
659 CNS. II. Behavior of pioneer growth cones. The Journal of neuroscience. 1989;9(7):2412-22.

660 31. Sink H, Whitington PM. Pathfinding in the central nervous system and periphery by
661 identified embryonic Drosophila motor axons. Development. 1991;112(1):307-16.

662 32. Landgraf M, Jeffrey V, Fujioka M, Jaynes JB, Bate M. Embryonic origins of a motor
663 system: motor dendrites form a myotopic map in Drosophila. PLoS biology. 2003;1(2):E41.

664 33. Pereanu W, Spindler S, Im E, Buu N, Hartenstein V. The emergence of patterned
665 movement during late embryogenesis of Drosophila. Dev Neurobiol. 2007;67(12):1669-85.

666 34. Arendt D, Tosches MA, Marlow H. From nerve net to nerve ring, nerve cord and
667 brain--evolution of the nervous system. Nature reviews Neuroscience. 2016;17(1):61-72.

668 35. Qing Yu ZL, Chuanzi OuYang, Lingjun Li. Biologically Active Peptides in
669 Invertebrates: Discovery and Functional Studies. Colloqium Series on neuropeptides:
670 Morgan & Claypool Publishers; 2015. p. 182.

671 36. Matheson T. Invertebrate Nervous Systems. Encyclopedia of Life Sciences. 2002:1-6.

672 37. Siechen S, Yang S, Chiba A, Saif T. Mechanical tension contributes to clustering of
673 neurotransmitter vesicles at presynaptic terminals. Proceedings of the National Academy
674 of Sciences of the United States of America. 2009;106(31):12611-6.

675 38. Franze K. The mechanical control of nervous system development. Development.
676 2013;140(15):3069-77.

677 39. Van Essen DC. A tension-based theory of morphogenesis and compact wiring in the
678 central nervous system. Nature. 1997;385(6614):313-8.

679 40. Hsieh MH, Nguyen HT. Molecular mechanism of apoptosis induced by mechanical
680 forces. International review of cytology. 2005;245:45-90.

681 41. Heiman MG, Shaham S. Twigs into branches: how a filopodium becomes a dendrite.
682 Curr Opin Neurobiol. 2010;20(1):86-91.

683 42. Bornstein B, Zahavi EE, Gelley S, Zoosman M, Yaniv SP, Fuchs O, et al. Developmental
684 Axon Pruning Requires Destabilization of Cell Adhesion by JNK Signaling. Neuron.
685 2015;88(5):926-40.

686 43. Baines RA, Bate M. Electrophysiological development of central neurons in the
687 Drosophila embryo. The Journal of neuroscience. 1998;18(12):4673-83.

688 44. Marder E, Bucher D. Central pattern generators and the control of rhythmic
689 movements. Curr Biol. 2001;11(23):R986-96.

690 45. Katz LC, Shatz CJ. Synaptic activity and the construction of cortical circuits. Science.
691 1996;274(5290):1133-8.

692 46. Kirkby LA, Sack GS, Firl A, Feller MB. A role for correlated spontaneous activity in
693 the assembly of neural circuits. Neuron. 2013;80(5):1129-44.

694 47. Hebb D. The Organization of Behavior: A Neuropsychological Theory. John Wiley
695 and Sons Inc; New York; Chapman and Hall Limited; London; 1949.

696 48. Eglen SJ, Demas J, Wong RO. Mapping by waves. Patterned spontaneous activity
697 regulates retinotopic map refinement. Neuron. 2003;40(6):1053-5.

698 49. Heckscher ES, Zarin AA, Faumont S, Clark MQ, Manning L, Fushiki A, et al. Even-
699 Skipped(+) Interneurons Are Core Components of a Sensorimotor Circuit that Maintains
700 Left-Right Symmetric Muscle Contraction Amplitude. Neuron. 2015;88(2):314-29.

701 50. Keshishian H, Chiba A. Neuromuscular development in Drosophila: insights from
702 single neurons and single genes. Trends Neurosci. 1993;16(7):278-83.

703 51. Grueber WB, Jan LY, Jan YN. Tiling of the Drosophila epidermis by multidendritic
704 sensory neurons. Development. 2002;129(12):2867-78.

705 52. Rasse TM, Fouquet W, Schmid A, Kittel RJ, Mertel S, Sigrist CB, et al. Glutamate
706 receptor dynamics organizing synapse formation in vivo. Nat Neurosci. 2005;8(7):898-905.

707 53. Gerhard S, Andrade I, Fetter RD, Cardona A, Schneider-Mizell CM. Conserved neural
708 circuit structure across Drosophila larval development revealed by comparative
709 connectomics. Elife. 2017;6.

710 54. Patel NH. Imaging neuronal subsets and other cell types in whole-mount Drosophila
711 embryos and larvae using antibody probes. Methods in cell biology. 1994;44:445-87.

712 55. Schindelin J, Arganda-Carreras I, Frise E, Kaynig V, Longair M, Pietzsch T, et al. Fiji:
713 an open-source platform for biological-image analysis. Nat Methods. 2012;9(7):676-82.
714 56. Longair MH, Baker DA, Armstrong JD. Simple Neurite Tracer: open source software
715 for reconstruction, visualization and analysis of neuronal processes. Bioinformatics.
716 2011;27(17):2453-4.
717
718
719 **ACKNOWLEDGEMENTS**
720 We are extremely grateful to all colleagues that have provided us materials, training and
721 guidance throughout this work as well as for commenting on the manuscript. Amongst them we
722 like to specially thank Claude Desplan, Matthias Landgraf, Chris Doe, Andreas Prokop, Natalia
723 Sanchez-Soriano, Marta Zlatic, Albert Cardona and Irene Miguel-Aliaga. We also have to thank
724 our colleagues at the Parc Cientific de Barcelona, the Mechanobiology Institute of Singapore and
725 the Fleming Institute of Athens for their constant encouragement and support.
726
727

728 **FIGURE LEGENDS**

729

# Figure 1

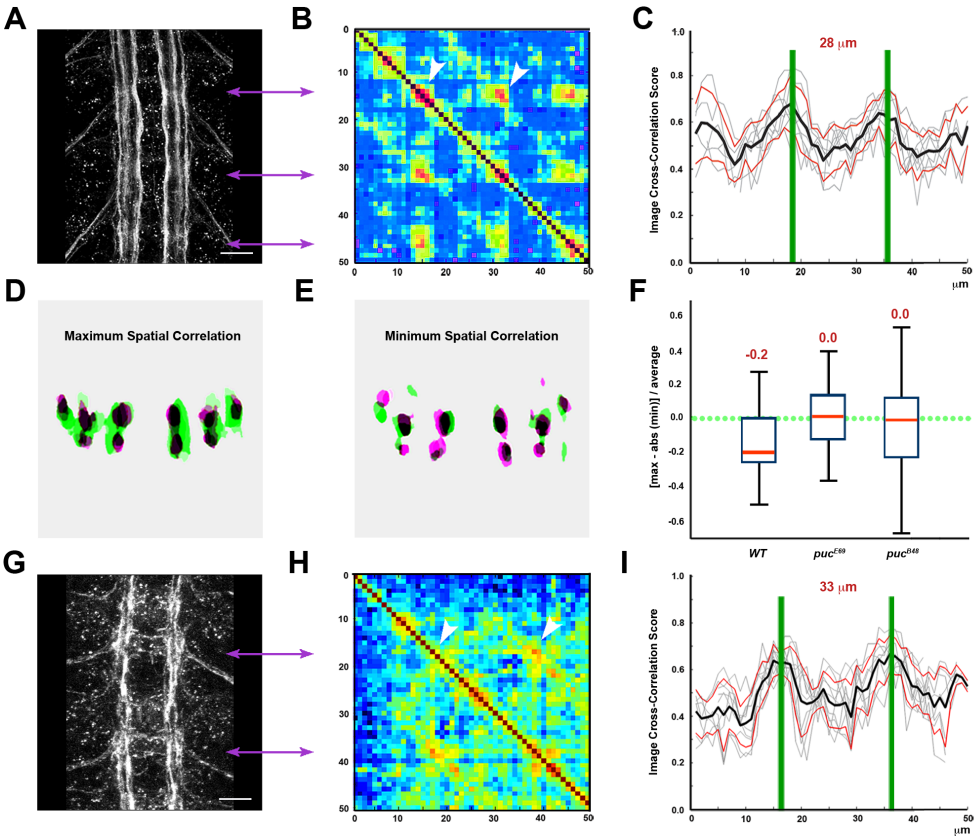


730

731

732

733 **Figure 1. Structural Architecture of the Ventral Nerve Cord (VNC) of the *Drosophila***
734 **embryo**

735 **A)** Maximum projection of the VNC of a *Drosophila* 16-stage *wt* embryo stained with Fas 2. See
736 **Movie S1**. Scale Bar is 10 μm.

737 **B)** Self cross-correlation matrix of the Z sections of the image in **A** along the A/P axis. The
738 color-coded representation, in all figures from now on, shows the correlation level for each
739 possible comparison at each position along the A/P axis. In this way it was possible to identify an
740 oscillatory pattern of hot spots (3D nodes - purple double headed arrows) of high correlation.
741 One conspicuous node of robust correlation per segment is detected (white arrowheads).

742 **C)** Image cross-correlation score along the A/P axis for **B**. The cross-correlation profile shows
743 that segmental Fas 2 nodes fell 28 μm apart in *wt* animals and that the internodal maximum
744 noise/minimum correlation maps 9 μm posterior to the node.

745 **D)** Z sections at two different maximal (green and magenta) correlation positions (from **A**)
746 showing coalescence of Fas 2 connectives at the nodes.

747 **E)** Z sections at two different minimal (green and magenta) correlation positions (from **A**)
748 showing dispersion and stochastic distribution associated to internodal noise.

749 **F)** Box plots of the differences vs. the mean for the variable r = [max (grad) - abs (min (grad))] /
750 [(max (grad) + abs (min (grad))) / 2] between datasets for *wt*, $puc^{E69}$ and $puc^{B48}$ individuals. The
751 median from *wt* was clearly less than zero with a 95% confidence interval. For the mutants this
752 was lost, with the values not distinguishable from zero. The bias in *wt* values indicates that the
753 decay in robustness from nodes in the posterior direction is more pronounced than its recovery
754 towards subsequent nodes. This behavior is abolished in $puc^{E69}$ and $puc^{B48}$.

755 **G)** Equivalent image to **A** for a $puc^{E69}$ embryo. Note the defasciculation and collapse of the
756 longitudinal connectives, specially the most lateral ones. See **Movie S2**. Scale Bar is 10 μm.

757 **H)** Self cross-correlation matrix of the Z sections of the image in **D**. In $puc^{E69}$ mutants, while
758 correlation matrices are noisier, a single node per segment can still be observed (white
759 arrowheads).

760 **I)** Image cross-correlation score along the A/P axis for **E**. Segmental Fas 2 nodes spread 33 μm
761 away in $puc^{E69}$ and the internodal minima gets diffuse.

# Figure 2

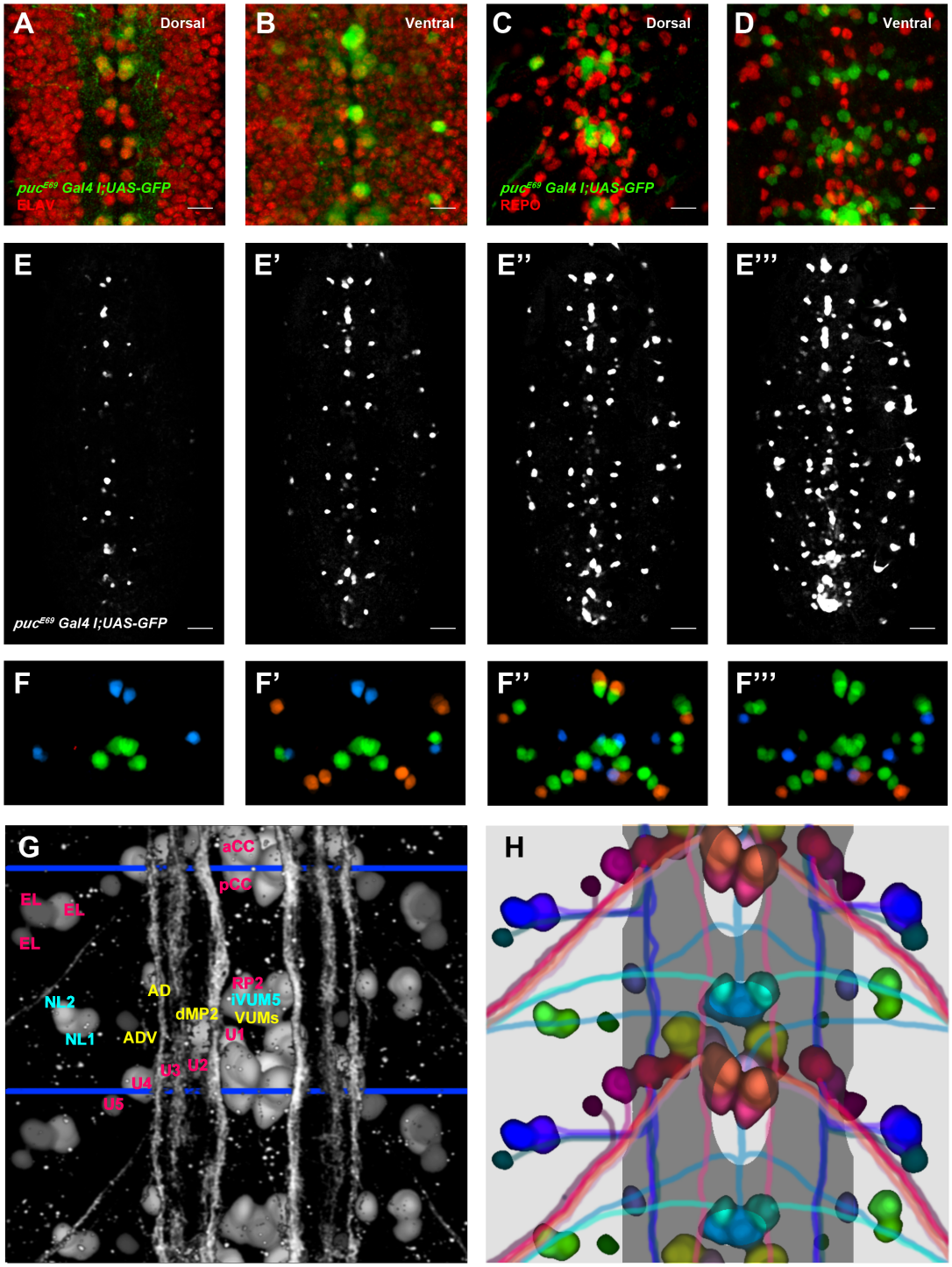
A
Dorsal
puc$^{E69}$ Gal4 I;UAS-GFP
ELAV
B
Ventral
C
Dorsal
puc$^{E69}$ Gal4 I;UAS-GFP
REPO
D
Ventral
E
E'
E''
E'''
puc$^{E69}$ Gal4 I;UAS-GFP
F
F'
F''
F'''
G
aCC
pCC
EL
EL
EL
NL2
NL1
AD
ADV
dMP2
RP2
iVUM5
VUMs
U1
U2
U3
U4
U5
H

762

763 **Figure 2. JNK signaling is dynamically regulated during development**

764 **A** to **D)** Dorsal and ventral sections highlighting the expression of *puc* (green) in the VNC of
765 stage 17 UAS-GFP; $puc^{E69}$*I*-Gal4 embryo double-stained for the pan-neuronal marker Elav (**A**
766 and **B** - red) or the glial marker Repo (**C** and **D** - red). *puc* is expressed in a subset of neurons in
767 each segments but not in glia. Scale Bar is 10 µm.

768 **E** to **E''')** four different snapshots from **Movie S3** at the indicated time points from the UAS-
769 GFP; $puc^{E69}$*I*-Gal4 viable line. *puc* expression can be observed from early stage 13 in a few
770 neurons at midline. As development progressed, more and more neurons express *puc*. Scale Bar
771 is 10 µm.

772 **F** to **F''')** Diagram displaying the cumulative expression of *puc* at the same time points as in **E** to
773 **E'''**. A minimum consensus of 19 neurons per hemisegment was defined. At each time point the
774 intensity (defined by visual inspection) was displayed as low (red), medium (blue) and high
775 (green) (see also **Movie S4**).

776 **G)** Composition summarizing the expression of *puc* in the CNS [*puc* expressing cells in the VNC
777 at stage 16 including those identified by coexpressing Even-skipped (magenta) or Engrailed
778 (cyan) plus those putatively identified by morphological and positional criteria (yellow - AD,
779 ADV, dMP2 and 2 VUM En-negative motor neurons)]. To facilitate understanding, a scaled Fas
780 2 expression image from an embryo of the same stage was overimposed to the diagram. Positions
781 of the robustness nodes are highlighted as dark blue lines.

782 **H)** Diagram representing the whole set of *puc* expressing cells (compare to G) and their expected
783 axonal contributions to connectives and exiting nerves (each individual cell carried a single
784 color-code). This diagram was over-imposed over a grey mask covering the scaled width and
785 shape of the VNC.

# Figure 3

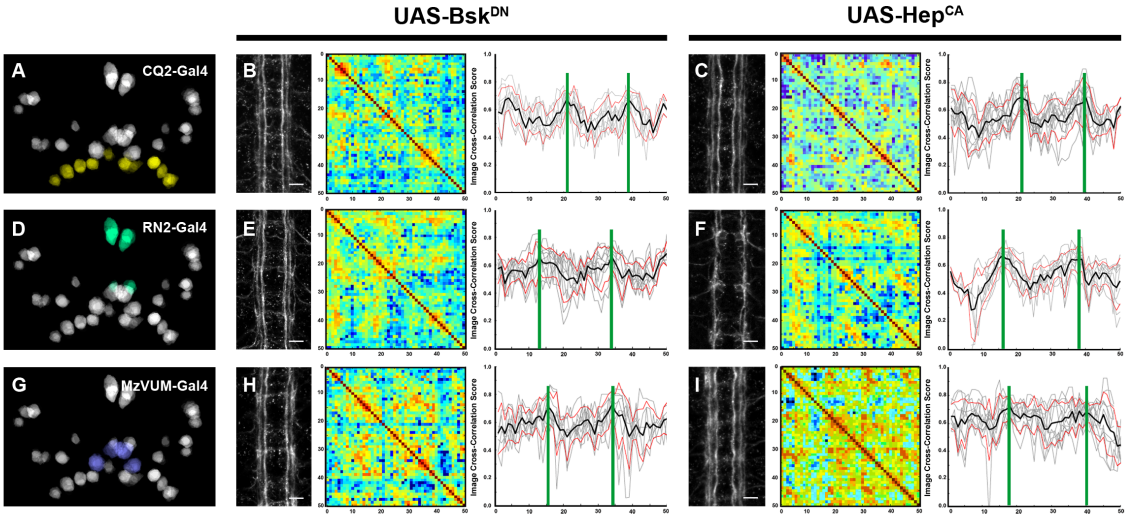
UAS-Bsk^DN
UAS-Hep^CA
A
CQ2-Gal4
B
C
D
RN2-Gal4
E
F
G
MzVUM-Gal4
H
I
Image Cross-Correlation Score

786

787 **Figure 3. Targeted activation and inhibition of the JNK pathway in the VNC**

788 **A)** Cartoon representing the full set of *puc* expressing neurons per segment in the VNC
789 highlighting the cells expressing CQ2-Gal4 (yellow).

790 **B** and **C)** From left to right, pattern of Fas 2 expression, self cross-correlation matrix and image
791 cross-correlation profiles for VNCs of 16-stage embryos upon expression of UAS-Bsk$^{DN}$ **(B)** and
792 UAS-Hep$^{CA}$ **(C)** transgenes under the control of the CQ2-Gal4 respectively inhibiting and
793 hyperactivating JNK activity in the U motoneurons. None of these conditions result in noticeable
794 defects. Scale Bar is 10 µm.

795 **D)** Cartoon highlighting the *puc* positive cells expressing RN2-Gal4 (turquoise).

796 **E** and **F)** As **B** and **C** but employing RN2-Gal4 for interfering in JNK activity in the aCC, pCC
797 and RP2 cells. Affecting JNK activity levels in aCC, pCC and RP2 cells affect connectives
798 defasciculation, nodes profiles and VNC condensation. Scale Bar is 10 µm.

799 **G)** Cartoon highlighting the *puc* positive neurons expressing MzVum-Gal4 (purple).

800 **H** and **I)** As **B** and **C** but employing MzVum-Gal4 for interfering in JNK activity in the VUM
801 neurons. Affecting JNK activity levels in VUMs also affects defasciculation, profiles and
802 condensation. Scale Bar is 10 µm.

803

# Figure 4

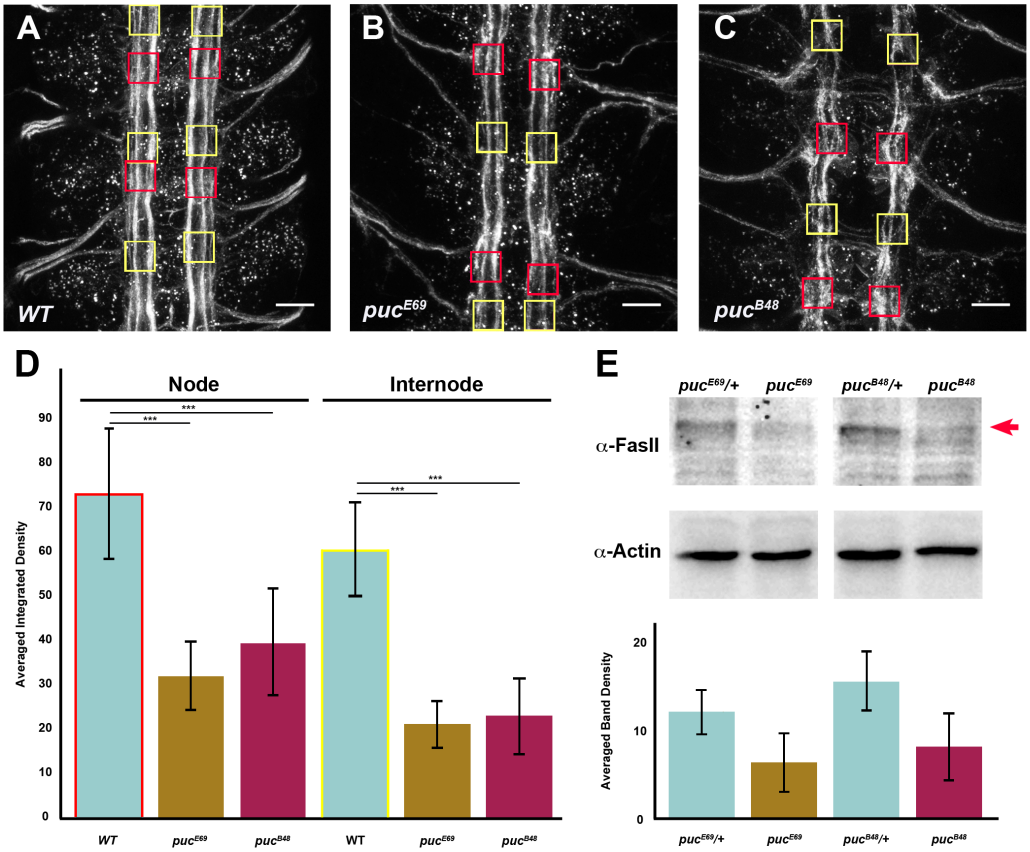
A
WT
B
pucE69
C
pucB48
D
Node
Internode
Averaged Integrated Density
0
10
20
30
40
50
60
70
80
90
***
***
***
***
WT
pucE69
pucB48
WT
pucE69
pucB48
E
pucE69/+
pucE69
pucB48/+
pucB48
α-FasII
α-Actin
Averaged Band Density
0
10
20
pucE69/+
pucE69
pucB48/+
pucB48

804

805 **Figure 4. Fasciclin 2 expression is reduced in *puc* mutants**

806 **A)** *wt*, **B)** $puc^{E69}$ and **C)** $puc^{B48}$ stage 16 embryos Fas 2 immunoreactivity. Maximum projection
807 of ventral views across three VNC abdominal segments. Overlaid squares represent the fixed
808 area ROIs used for measuring the Average Integrated Density of Fas 2 signal, either at the node
809 (red) or at the internode (yellow) positions. Scale Bar is 10 µm.

810 **D)** Quantification of the Average Integrated Density of Fas 2 signal at node and internode
811 positions as indicated. Statistically significant differences in Fas 2 levels ($p < 0.0001$) were
812 detected between *wt* and *puc* embryos, both at the node and internode positions.

813 **E)** Immunodetection of Fas 2 in extracts from stage 16 *puc* embryos. Extracts of balanced
814 siblings were used as controls. In control extracts, the antibody against Fas 2 detected a strong
815 band at 95 kD (red arrow), the intensity of which was reduced by half in extracts from *puc*
816 homozygous embryos. Detection of actin (42 kD) served as loading control for the quantification
817 of the Fas 2 signal. The graph represents the averaged Fas 2 band intensities normalized with
818 respect to actin.

819

# Figure 5

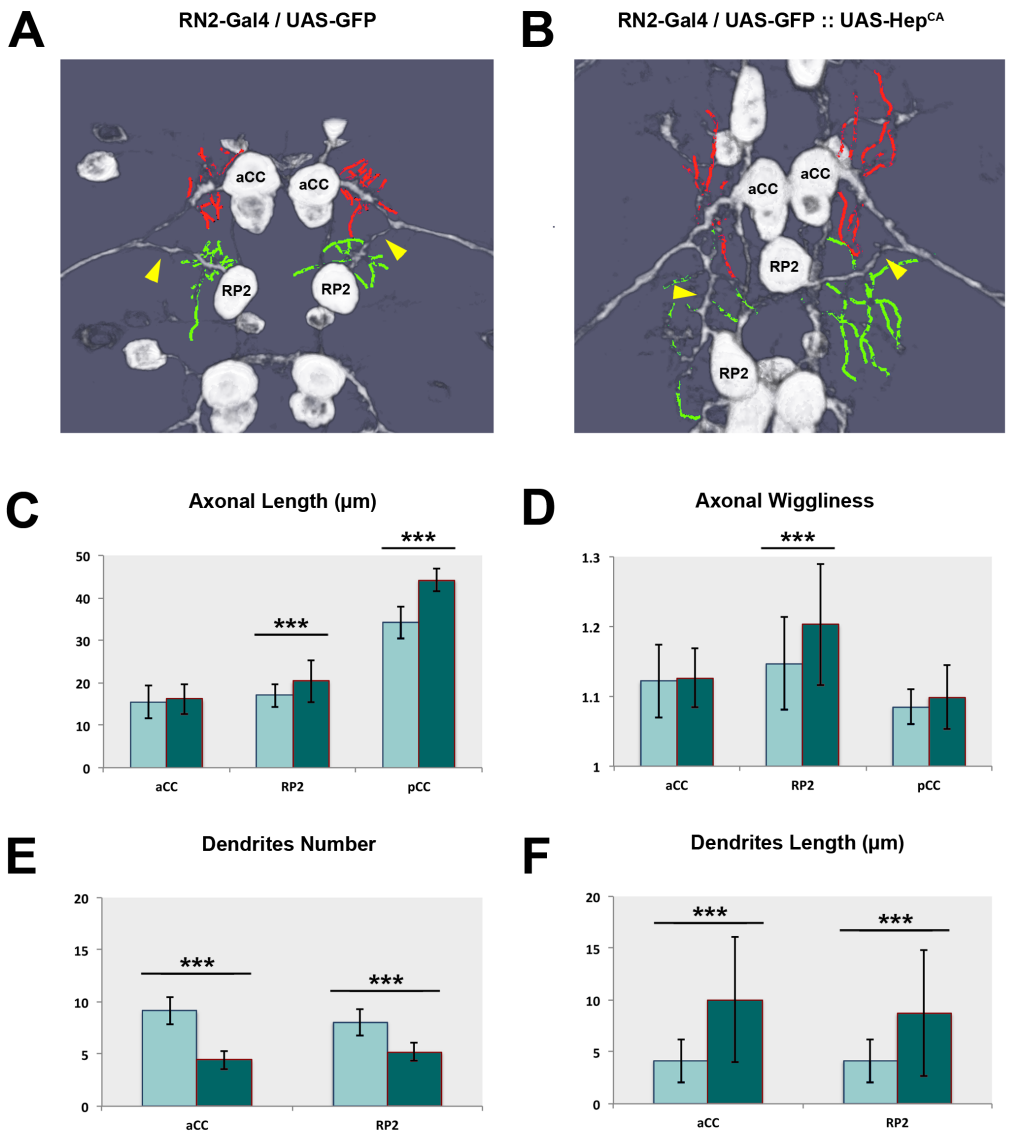
A
RN2-Gal4 / UAS-GFP
aCC
aCC
RP2
RP2
B
RN2-Gal4 / UAS-GFP :: UAS-Hep^CA
aCC
aCC
RP2
RP2
C
Axonal Length (µm)
***
***
50
40
30
20
10
0
aCC
RP2
pCC
D
Axonal Wiggliness
***
1.3
1.2
1.1
1
aCC
RP2
pCC
E
Dendrites Number
***
***
20
15
10
5
0
aCC
RP2
F
Dendrites Length (µm)
***
***
20
15
10
5
0
aCC
RP2

820

821 **Figure 5. Pioneer neurons axonal and dendritic landscape is altered upon JNK hyper-**
822 **activation**

823 **A** and **B**) Flat-prepped, stage 16 embryos expressing mCD8-GFP (**A**) and mCD8-GFP and
824 $Hep^{CA}$ (**B**) under the control of the RN2-Gal4 line immunostained for GFP. Traces of the aCC
825 (red) and RP2 (green) proximal dendrites are over-imposed. Yellow arrowheads point to
826 differences in RP2 axon morphology. Anterior is up. Scale bar is 10 µm.

827 **C**) Histograms showing the average axonal length of the aCC, RP2 and pCC neurons.
828 Statistically significant differences ($p<0.001$) in the axonal length of the RP2 and pCC neurons
829 were detected between control and $Hep^{CA}$ expressing neurons (n= 4 embryos). Control embryos
830 are represented in light green and $Hep^{CA}$ expressing embryos in dark green.

831 **D**) Histograms showing the average axonal wiggliness of the aCC, RP2 and pCC neurons. RP2
832 axonal wiggliness was found significantly increased after $Hep^{CA}$ expression ($p<0.001$, n= 4
833 embryos).

834 **E** and **F**) Graphs representing the average Dendrite Number (**E**) and average Dendrite Length (**F**)
835 of the aCC and RP2 neurons. In all cases significant differences were scored in the comparison
836 of control and $Hep^{CA}$ expressing embryos ($p<0.001$, n= 4 embryos).

837

# Figure 6

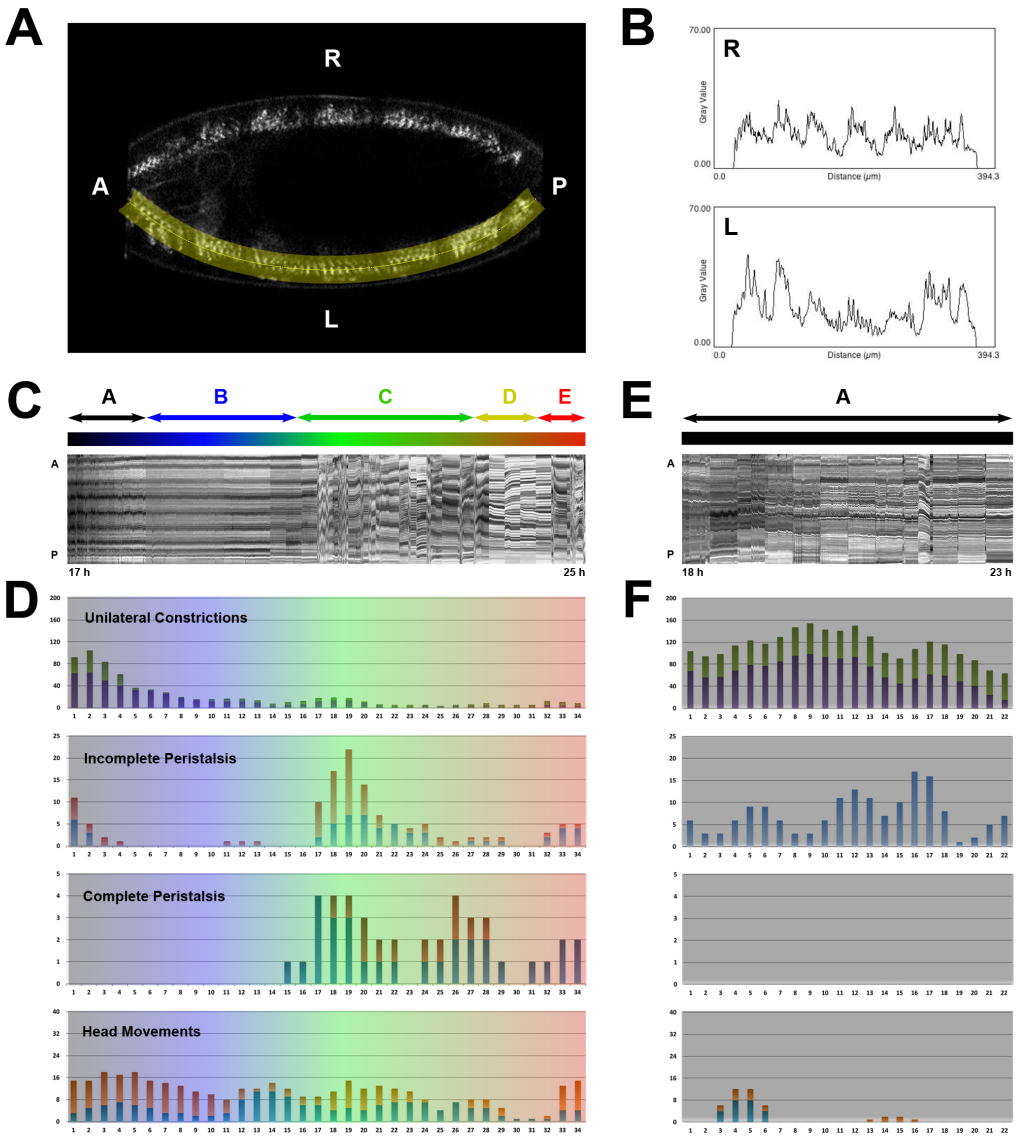
A
R
A
P
L
B
R
70.00
Gray Value
0.00
0.0
Distance (μm)
394.3
L
70.00
Gray Value
0.00
0.0
Distance (μm)
394.3
C
A
B
C
D
E
A
P
17 h
25 h
E
A
A
P
18 h
23 h
D
Unilateral Constrictions
Incomplete Peristalsis
Complete Peristalsis
Head Movements
F

838

839 **Figure 6. Defective motor coordination results in the absence of complete peristalsis in**
840 ***puc*$^{E69}$ embryos**

841 **A)** Representative mid-plane image of a stage 17 embryo carrying two GFP protein traps
842 expressed at muscle Z-lines (w; G203, ZCL2144) (see **Movie S7**). A selected segmented-line
843 (highlighted in yellow) was employed to create kymographs spanning muscle units along the
844 antero-posterior (A/P) axis (see below) at both sides of the embryo, right (R) and left (L). The
845 evolution overtime of these kymographs was monitored live. Scale bar is 50 µm.

846 **B)** Intensity Profile plots generated along the segmented-line selection in **A**. Gray values as a
847 function of distance highlight the distribution of the segmental muscle units along the axis.
848 Muscle contraction is detected by the differences in the distance between consecutive peaks at
849 sequential time points.

850 **C)** Kymograph displaying muscle units profiles from 17 to 25 hours AEL for the left side of the
851 embryo in **A**. Anterior (A) and posterior (P). Motor coordination maturation occurs in 5 stages of
852 approximated stereotyped length (color coded): A, Intense unilateral twitching; B, general
853 inactivity with occasional uncoordinated contractions; C, initiation of backward and forward
854 peristalsis; D, pre-hatching inactivity period and E, complete peristalsis and specialized hatching
855 head movements.

856 **D)** Histograms showing the progression of the muscle coordination process in wild type
857 embryos. Over-imposed colors follow the 5 stages of motor coordination maturation described in
858 **C**. Muscle movements were distributed in four classes: Unilateral contractions [sum of the
859 contractions occurring at the right (green) and the left (purple) side of the embryo]; Incomplete
860 peristalsis [sum of the incomplete forward (blue) and incomplete backward (red) peristaltic
861 attempts]; Complete peristalsis [sum of the full forward (blue) and backward (red) peristalsis];
862 and Head movements [sum of head turning (red) and mouth hook pinching events (blue)].

863 **E)** Kymograph displaying muscle units profiles from 18 to 23 hours AEL, when the embryo dies,
864 for the left side of a *puc*$^{E69}$ embryo (see **Movie S8**). Anterior (A) and posterior (P). Motor
865 coordination fails and embryos do not progress beyond the unilateral contraction period (stage
866 A).

867 **F)** Histograms equivalent to **D** showing the unsuccessful muscle coordination of *puc*$^{E69}$ embryos.

868

# Figure 7

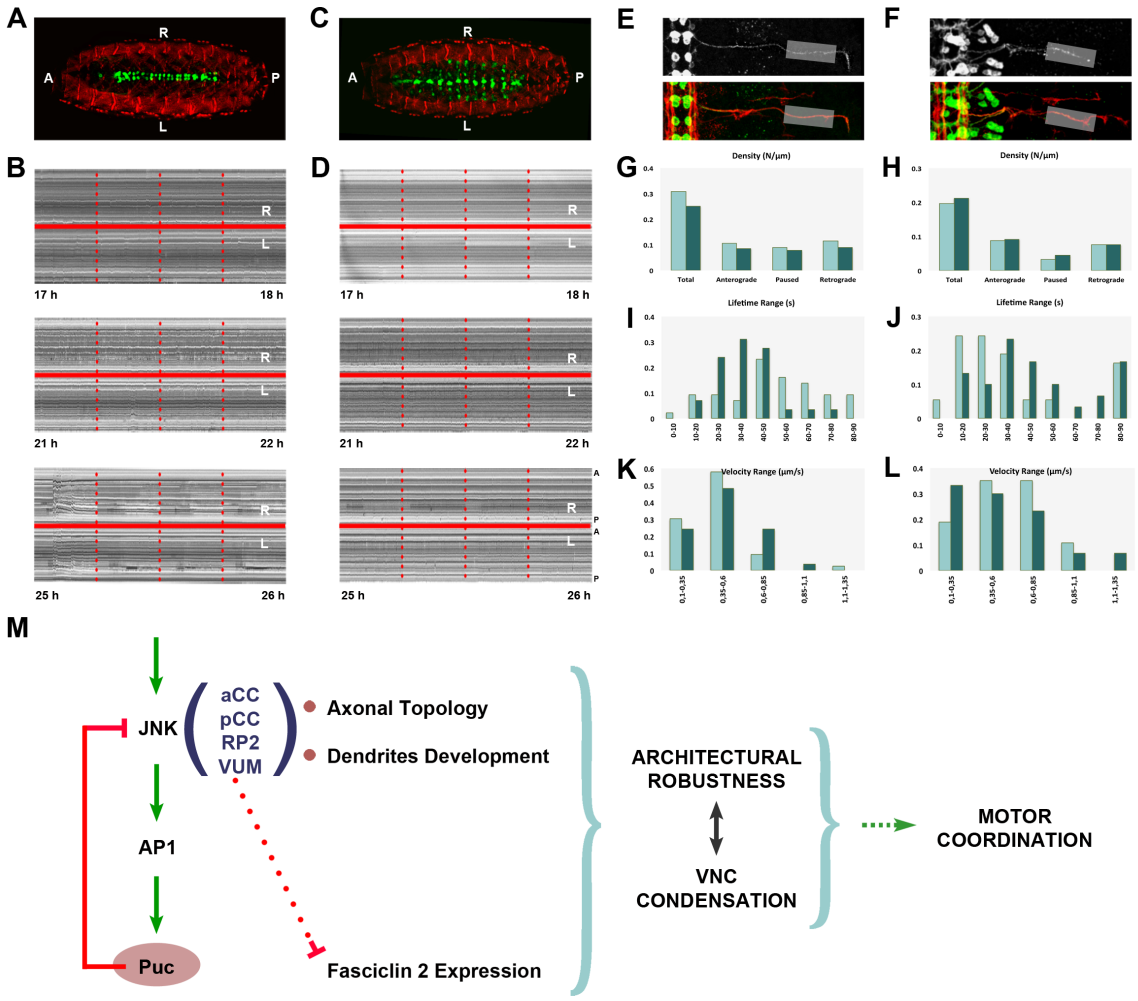
A
R
A
P
L
C
R
A
P
L
E
F
B
R
L
17 h
18 h
21 h
22 h
25 h
26 h
D
R
L
17 h
18 h
21 h
22 h
25 h
26 h
A
P
A
P
G
Density (N/µm)
Total
Anterograde
Paused
Retrograde
H
Density (N/µm)
Total
Anterograde
Paused
Retrograde
I
Lifetime Range (s)
0-10
10-20
20-30
30-40
40-50
50-60
60-70
70-80
80-90
J
Lifetime Range (s)
0-10
10-20
20-30
30-40
40-50
50-60
60-70
70-80
80-90
K
Velocity Range (µm/s)
0,1-0,35
0,35-0,6
0,6-0,85
0,85-1,1
1,1-1,35
L
Velocity Range (µm/s)
0,1-0,35
0,35-0,6
0,6-0,85
0,85-1,1
1,1-1,35
M
JNK
aCC
pCC
RP2
VUM
Axonal Topology
Dendrites Development
AP1
Puc
Fasciclin 2 Expression
ARCHITECTURAL ROBUSTNESS
VNC CONDENSATION
MOTOR COORDINATION

869

870 **Figure 7. JNK activity modulates VNC condensation and embryo motor coordination but**
871 **does not affect synaptic vesicles transport**

872 **A** and **C)** Ventral view of stage 17 embryos expressing GFP under the control of the RN2-Gal4
873 (**A**) and MzVum-Gal4 (**C**) lines carrying the muscle Z-lines specific GFP protein trap ZCL2144.
874 Muscles are pseudo-colored in red and neurons in green. Scale bar is 50 µm.

875 **B** and **D**) Kymographs (ZCL2144 marker) revealing occasional unilateral contractions in
876 embryos co-expressing $Hep^{CA}$ in the RN2-Gal4 (**B**) and MzVum-Gal4 (**D**) neurons. For each
877 case, the kymographs correspond to three periods of 1 hour. These embryos never manage to
878 coordinate muscle movements. Both sides, right (R) and left (L) are shown.

879 **E** and **F**) Flat-prepped, stage 16 embryos expressing syt-GFP under the control of the RN2-Gal4
880 (**E**) and MzVum-Gal4 (**F**) lines immunostained against GFP (grayscale - top panels and green -
881 bottom panels) and Fas 2 (red - bottom panel). The grey rectangle marks the medial part of the
882 ISN, where synaptic vesicles axonal transport was monitored (see **Movie S9**). Scale bar is 25
883 µm.

884 **G** and **H**) Histograms showing synaptotagmin vesicles density and directional motility in control
885 (light green) versus $Hep^{CA}$ expressing (dark green) aCC/ RP2 (**G**) and VUM motoneurons (**H**).
886 No statistically significant differences were observed between control and JNK over-active
887 neurons.

888 **I** and **J**) Lifetime range distribution of motile synaptotagmin vesicles in aCC/RP2 (**I**) and VUM
889 (**J**) motoneurons. No differences were observed in lifetime between control (light green) and
890 $Hep^{CA}$ expressing (dark green) embryos.

891 **K** and **L**) Mean velocity range distribution comparison of motile synaptotagmin vesicles in
892 aCC/RP2 (**K**) and VUM (**L**) motoneurons between control (light green) and JNK gain-of
893 function (dark green) conditions. For both sets of motoneurons the distribution was unaltered.

894 **M)** Regulatory network modulating VNC architectural robustness and condensation and
895 coordinating motor activities. Precise JNK activity levels in early-specified neurons (at least
896 aCC, pCC, RP2 and VUMs) are regulated by a negative feedback loop mediated by Puc.
897 Excessive JNK activity in *puc* mutants or upon overexpressing HepCA in aCC, pCC, RP2 and/or
898 VUMs leads to autonomous defects in axonal paths and dendrites numbers and shape. It also
899 results in a general downregulation of Fas 2 expression (autonomous and non-autonomous)

(discontinuous red inhibitory sign). As a result, the architectural robustness of the VNC will be affected and its condensation prevented. Further, the coordination of embryonic motor activities and peristaltic movements are also inhibited. This could be in part consequence of a failure in wiring optimization arising from the incomplete condensation of the VNC (discontinuous green arrow).

908 **SUPPLEMENTAL FIGURES LEGENDS**

# Figure S1

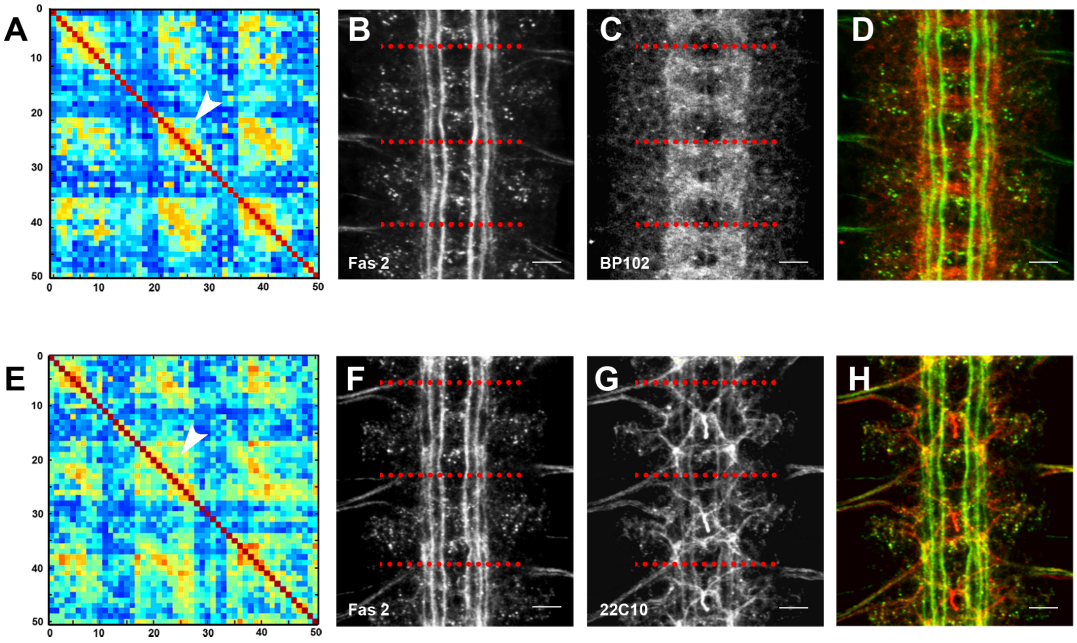


909

910 **Figure S1. Fine localization of robustness nodes**

911 **A)** Self cross-correlation matrix of the Z sections of the image in **B**. A conspicuous node of
912 robust correlation is highlighted (white arrowhead).

913 **B** to **D)** Images for Fas 2 (**B** - green in **D**), BP102 (**C** - red in **D**) and their superimposed image
914 (**D**) of a double-stained 16 stage *wt* embryo. Discontinued red lines indicate the localization of
915 the robustness nodes in relation to the VNC pattern. Scale Bar is 10 µm.

916 **E)** Self cross-correlation matrix of the Z sections of the image in **F**. A conspicuous node of
917 robust correlation is highlighted (white arrowhead).

918 **F** to **H)** Images for Fas 2 (**F** - green in **H**), 22C10 (**G** - red in **H**) and their superimposed image
919 **(H)** of a double-stained 16 stage *wt* embryo. Discontinued red lines indicate the localization of
920 the robustness nodes in relation to the VNC pattern. Scale Bar is 10 µm.

921

# Figure S2

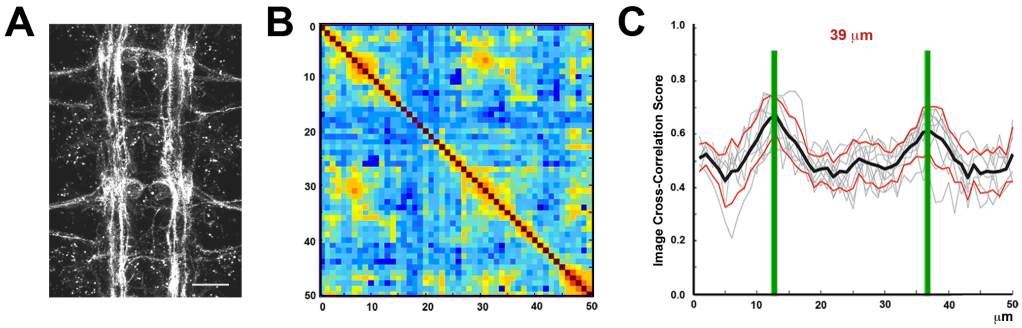


922

923 **Figure S2. Robustness and modularity of the VNC architecture in *puc$^{B48}$* embryos**

924 **A)** Maximum projection of the VNC of a *Drosophila* 16-stage *puc$^{B48}$* embryo stained with Fas 2.
925 Defasciculation and collapse of longitudinal connectives is widely spread. Scale Bar is 10 μm.

926 **B)** Self cross-correlation matrix of **A**. In *puc$^{B48}$*, single nodes per segment are consistently
927 developed (white arrowheads).

928 **C)** Image cross-correlation score along the A/P axis for **B**. Segmental Fas 2 nodes are on average
929 at 39 μm from each other in *puc$^{B48}$* and the internodal profile flattens.

930

# Figure S3

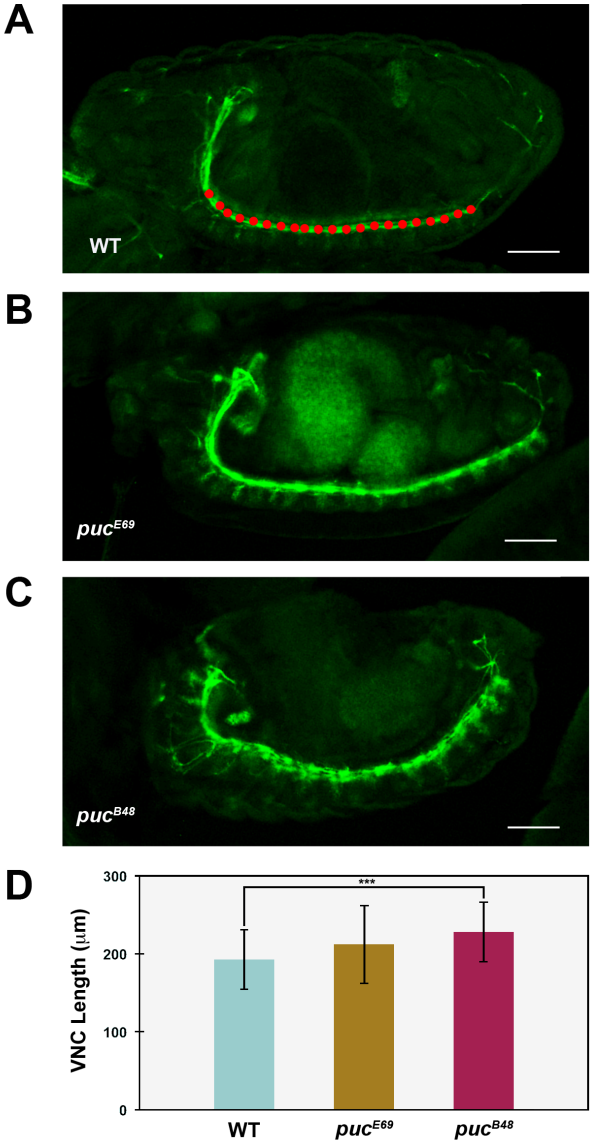


931

932 **Figure S3. Loss of VNC condensation in *puc* mutants**

933 **A)** *wt*, **B)** $puc^{E69}$ and **C)** $puc^{B48}$ embryos Fas 2 immunoreactivity. Lateral view of whole mounts
934 of stage 17 embryos. Direct measurements of the VNC length were performed along the outline
935 of the abdominal segments of the VNC as shown in A (dotted red line). Scale Bar is 10 μm.

936 **D)** Quantification of the VNC in μm (average and standard deviation) for each condition.
937 Statistically significant differences in length ($p < 0.001$) were detected between the *wt* and $puc^{B48}$
938 embryos. The length of the VNC of $puc^{E69}$ embryos showed a tendency to be consistently longer
939 than the *wt*, although it was not statistically significant.

940

# Figure S4

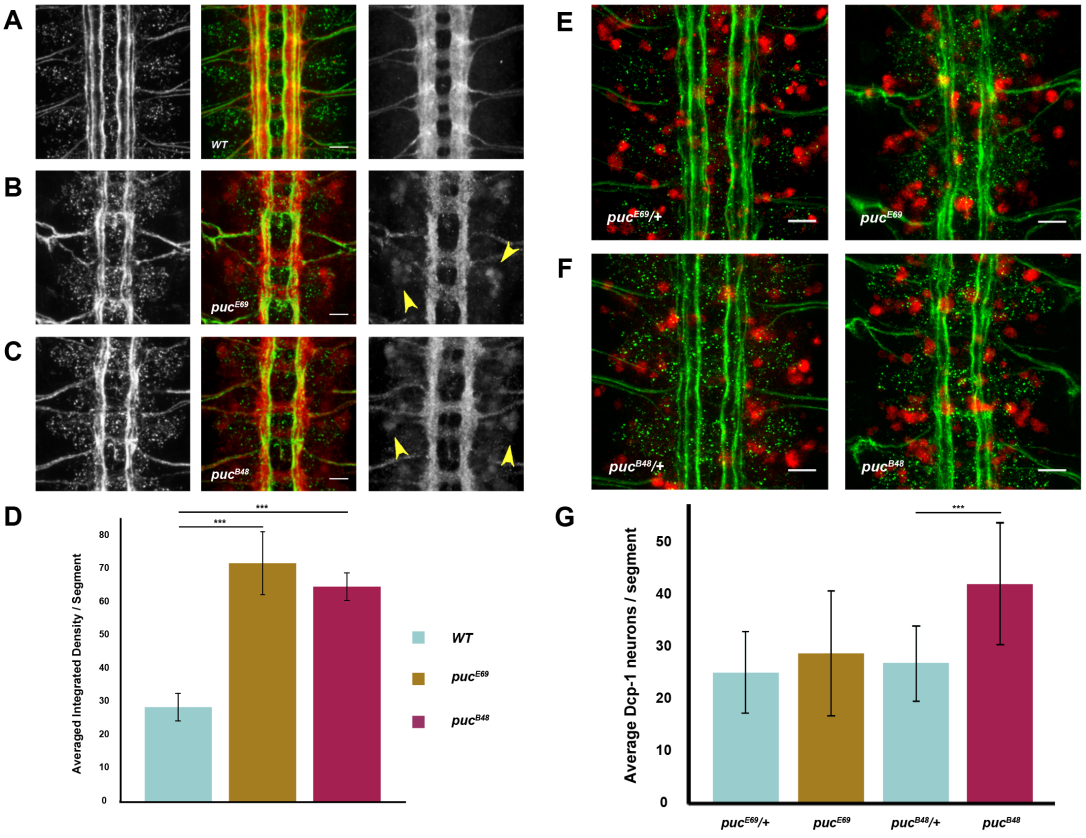


941

942 **Figure S4. JNK activity and Cell Death in *puc* mutants**

943 **A)** Single (left and right) and combined (centre) channels highlighting the expression of Fas 2
944 (left - green) and anti-P-JNK (right- red) of a stage 17 *wt* embryo. Scale Bar is 10 µm.

945 **B)** Equivalent as A for a stage 17 $puc^{E69}$ embryo. Scale Bar is 10 µm.

946 **C)** Equivalent as A for a stage 17 $puc^{B48}$ embryo. Scale Bar is 10 µm.

947 In mutant embryos (**B** and **C**) a significant fraction of the P-JNK signal remained in or around
948 cell bodies (yellow arrowheads) and is not strictly found as in *wt* only in axons.

949 **D)** Graph displaying the averaged Integrated Density per segment for the P-JNK signal.
950 Statistically significant differences in P-JNK levels ($p < 0.001$) were detected between the *wt* and
951 both mutant conditions.

952 **E)** From left to right, stage 17 heterozygous and homozygous $puc^{E69}$ embryo stained for Fas 2
953 (green) and Dcp1 (red), which highlights those cells in the process of apoptosis. Scale Bar is 10
954 µm.

955 **F)** From left to right, equivalent images as in **E** for the $puc^{B48}$ allele. Scale Bar is 10 µm.

956 **G)** Graph displaying the averaged Integrated Density per segment for the Dpc1 signal.
957 Statistically significant differences in Dcp1 levels ($p < 0.001$) were detected between *wt* and
958 $puc^{B48}$ embryos. The Dpc1 levels of $puc^{E69}$ embryos showed a tendency to be consistently larger
959 than in the *wt*, although they were not statistically significant.

960

# Figure S5

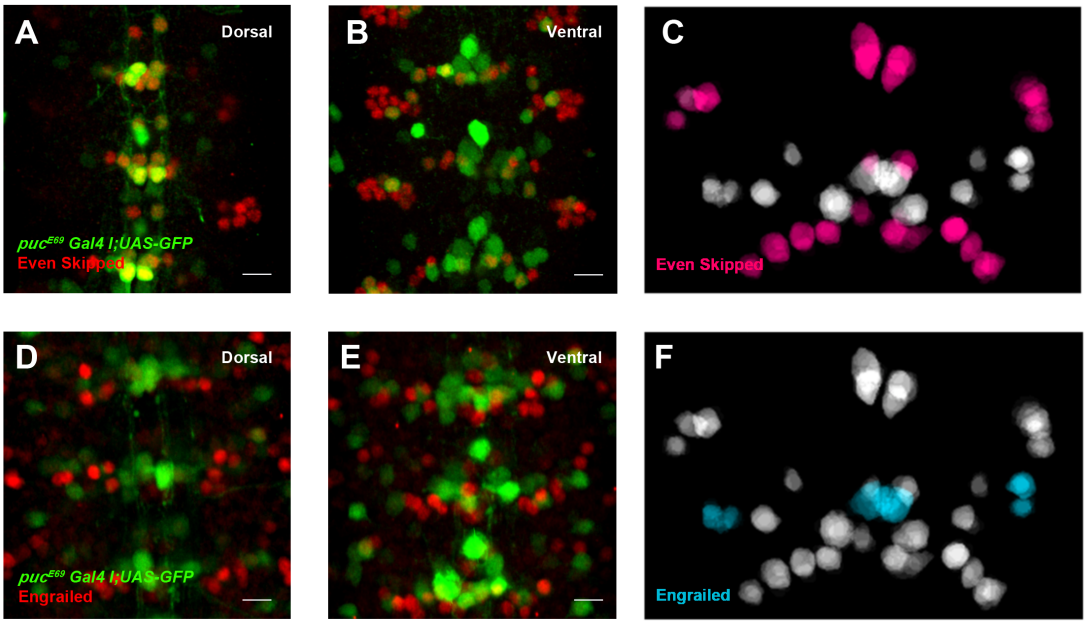


961

962 **Figure S5. Identities of *puc*-expressing neurons**

963 **A** and **B)** Dorsal and ventral sections highlighting the expression of *puc* (green) in the VNC of
964 stage 17 UAS-GFP; $puc^{E69}$*I*-Gal4 embryo double-stained for Even-Skipped (red). Scale Bar is 10
965 µm.

966 **C)** Diagram indicating those *puc* expressing cells also expressing Even-Skipped [magenta - aCC,
967 pCC, RP2, U1-U3 (plus weak/variable expression in U4-U5) and 3 out of the 8 to 10 EL
968 interneurons].

969 **D** and **E)** Dorsal and ventral sections highlighting the expression of *puc* (green) in the VNC of
970 stage 17 UAS-GFP; $puc^{E69}$*I*-Gal4 embryo double-stained for Engrailed (red). Scale Bar is 10 µm.

971 **F)** Diagram indicating those *puc*-expressing cells also expressing Engrailed (cyan - NL1, NL2,
972 and iVUM5 neurons).

973

# Figure S6

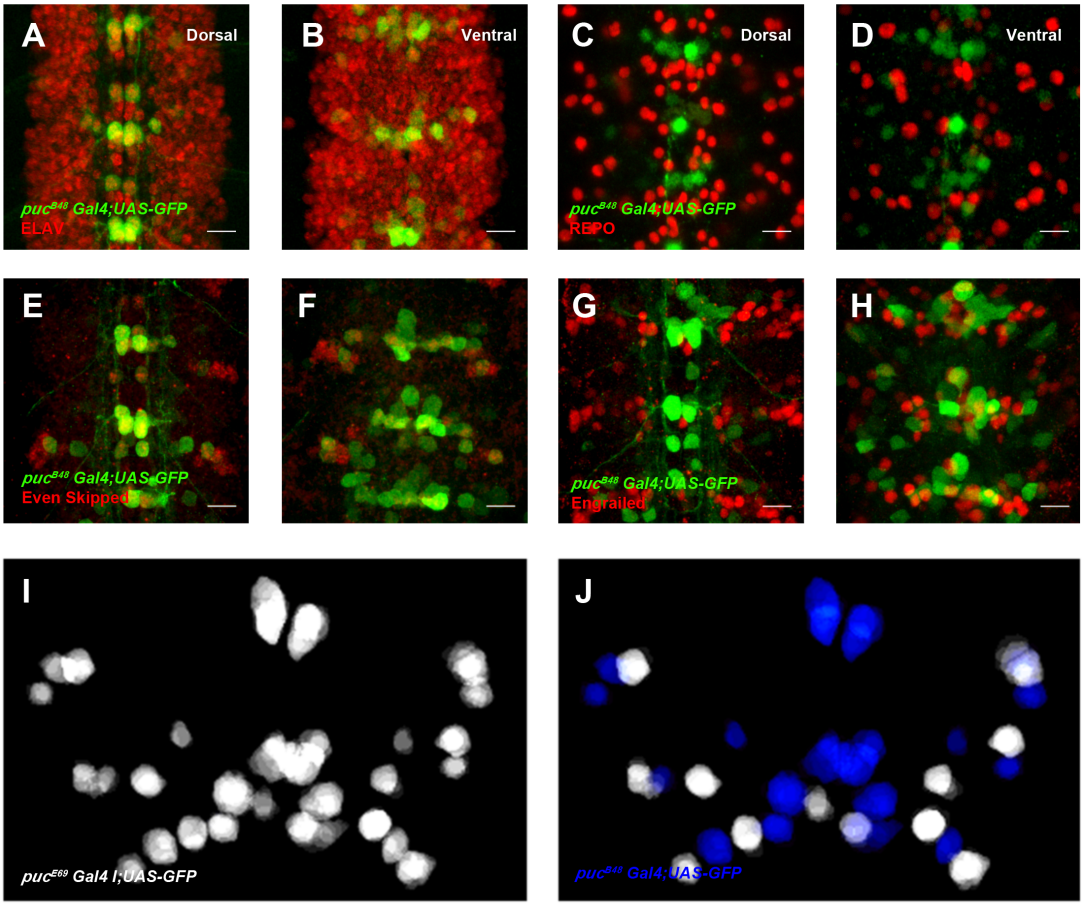


974

975 **Figure S6. *puc*$^{B48}$ expressing neurons**

976 **A** to **D)** Dorsal and ventral sections highlighting the expression of *puc* (green) in the VNC of
977 stage 17 UAS-GFP; *puc*$^{B48}$-Gal4 embryo double-stained for the pan-neuronal marker Elav (**A**
978 and **B** - red) or the glial marker Repo (**C** and **D** - red). *puc* is expressed in a subset of neurons in
979 each segments but not in glia. Scale Bar is 10 µm.

980 **E** to **H)** Dorsal and ventral sections highlighting the expression of *puc* (green) in the VNC of
981 stage 17 UAS-GFP; *puc*$^{B48}$-Gal4 embryo double-stained for Even-Skipped (**E** and **F** - red) or
982 Engrailed (**G** and **H** - red). Scale Bar is 10 µm.

983 **I)** Cartoon representing the full set of *puc*$^{B48}$ expressing neurons per segment in the VNC.

984 **J)** Cartoon representing the *puc*$^{E69}$ neurons highlighting the cells expressing *puc*$^{B48}$ (deep blue).

985

# Figure S6

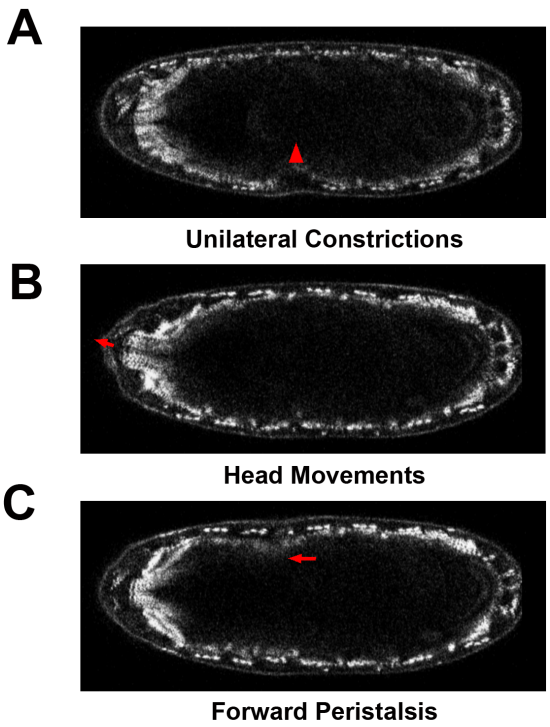


986

987 **Figure S7. Types of embryonic muscles movements**

988 Snapshots from **Movie S6** displaying mid-plane images of a stage 17 embryo carrying two GFP
989 protein traps expressed at muscle Z-lines (w; G203, ZCL2144). Three main types of movement
990 were observed during the muscle coordination process. Red arrows point to the contracting
991 muscle units. Anterior is to the left. Scale bar is 50 µm.

992 **A)** Unilateral muscle contractions. They can occured at any embryo side and in different
993 segments.

994 **B)** Head turning and mouth hook pinching.

995 **C)** Peristalsis. They can be incomplete or complete and develop forward (in the image) or
996 backward displacements.

997

998

999 **SUPPLEMENTAL MOVIES LEGENDS**

1000

1001 **Movie S1. *Drosophila* Fas 2 positive connectives**

1002 Animated 3D reconstruction of the Fas 2 positive connectives of a section of the VNC of a late
1003 *Drosophila* embryo (Stage 17).

1004

1005 **Movie S2. *Drosophila* Fas 2 positive connectives of a $puc^{E69}$ embryo**

1006 Animated 3D reconstruction of the Fas 2 positive connectives of a section of the VNC of a late
1007 *Drosophila* $puc^{E69}$ mutant embryo (Stage 17).

1008

1009 **Movie S3. Dynamics of $puc^{E69}$ expression**

1010 Time course of $puc^{E69}$ expression from a UAS-GFP; $puc^{E69}$*I*-Gal4 viable line. *puc* expression can
1011 be observed from early stage 13 in a few neurons at the midline. As development progressed,
1012 more and more neurons express *puc*, both within the VNC and at the peripheral nervous system
1013 (PNS). Scale bar is 50 µm. Anterior is to the left.

1014

1015

1016 **Movie S4. Minimum consensus for the segmental *puc$^{E69}$* expression**

1017 Animated 3D cartoon representing a single segment of a late *Drosophila puc$^{E69}$* mutant embryo
1018 (Stage 17). The 19 *puc* expressing cells per hemisegment represented in the minimum consensus
1019 are shown in different colors.

1020

1021 **Movie S5. Axonal and dendritic landscape of pioneer neurons upon JNK hyper-activation**

1022 Animated 3D reconstruction of the axonal and dendritic pattern of stage 16 embryos expressing
1023 mCD8-GFP (**A**) and mCD8-GFP and Hep$^{CA}$ (**B**) under the control of the RN2-Gal4 line. Traces
1024 of the dendrites (green) are over-imposed. Scale bar is 10 µm.

1025

1026 **Movie S6. Embryonic motor patterns**

1027 Representative mid-plane movies of a stage 17 embryo carrying two GFP protein traps expressed
1028 at muscle Z-lines (w; G203, ZCL2144). **A)** Forward peristalsis. **B)** Backward Peristalsis. **C)** Left
1029 twitch. **D)** Right twitch. **E)** Head tumble. **F)** Mandible pinch. Scale bar is 50 µm. Anterior is to
1030 the left.

1031

1032 **Movie S7. Time course of motor maturation**

1033 Representative mid-plane movies (250 time points per stage) of an embryo carrying two GFP
1034 protein traps expressed at muscle Z-lines (w; G203, ZCL2144). From top to bottom stages **A**
1035 (Unilateral twitches and incomplete peristalsis), **B** (Resting period), **C** (Complete peristalsis), **D**
1036 (Late resting period) and **E** (Hatching movements). Color coded as in **Figure 6**. Scale bar is 50
1037 µm. Anterior is to the left.

1038

1039 **Movie S8. Motor activity of *puc$^{E69}$* embryos**

1040 Representative mid-plane movie (1000 time points) of a late stage 17 *puc$^{E69}$* embryo carrying
1041 two GFP protein traps expressed at muscle Z-lines (w; G203, ZCL2144). Scale bar is 50 µm.
1042 Anterior is to the left.

1043

1044

1045 **Movie S9. Synaptic vesicles axonal transport in RN2 neurons**

1046 Stage 16 embryos expressing Synaptotagmin-GFP under the control of the RN2-Gal4 in the
1047 absence **(A)** or presence **(B)** of $Hep^{CA}$. Left panels present representative single plane movies
1048 (Fire Luts) with 1 sec interval for a total of 60 cycles. Right panels display in different colors the
1049 traces of the different particles analyzed. Proximal is to the left. Scale bar is 25 µm.

1050

1051